

AD-A049 347

BELL AEROSPACE TEXTRON BUFFALO N Y
ANALYTICAL STUDY TO MEASURE SOLAR RADIATION PRESSURE ON NTS-3 S--ETC(U)
AUG 77 M M MELDRUM, W G LANGE

F/G 3/2

F19628-77-C-0160

AFGL-TR-77-0215

NL

UNCLASSIFIED

1 OF 1

AD
A049347



END
DATE
FILMED
3 - 78

DDC

AD No. AD A049347

DDC FILE COPY

AFGL-TR-77-0215

ANALYTICAL STUDY TO MEASURE SOLAR
RADIATION PRESSURE ON NTS-3 SATELLITE
USING MESA ACCELEROMETER

Murray M. Meldrum
William G. Lange

Final Report

Period Covered: 1 May 1977 through 31 October, 1977

August 31, 1977

Approved for public release, distribution unlimited

Prepared For

Air Force Geophysics Laboratory
Air Force Systems Command
United States Air Force
Hanscom AFB, Massachusetts 01731

DDC
RECEIVED
FEB 2 1978
A

Qualified requestors may obtain additional copies from the Defense Documentation Center. All others should apply to the National Technical Information Service.

19 REPORT DOCUMENTATION PAGE		READ INSTRUCTIONS BEFORE COMPLETING FORM	
1. REPORT NUMBER (18) AFGL-TR-77-8215	2. GOVT ACCESSION NO. (Study)	3. RECIPIENT'S CATALOG NUMBER (Kept)	
4. TITLE (and Subtitle) (6) Analytical Studies to Measure Solar Radiation Pressure on NTS-3 Satellite Using MESA Accelerometer		5. TYPE OF REPORT & PERIOD COVERED (9) Final 1 May 1977 to 31 October 1977	
7. AUTHOR(s) (10) Murray M. Meldrum William G. Lange		6. PERFORMING ORG. REPORT NUMBER	
8. PERFORMING ORGANIZATION NAME AND ADDRESS Bell Aerospace TEXTRON P. O. Box One Buffalo, New York 14240		9. CONTRACT OR GRANT NUMBER(s) (15) F19628-77-C-8168	
11. CONTROLLING OFFICE NAME AND ADDRESS Air Force Geophysics Laboratory Hanscom AFB, Mass., 01731 Contract Monitor: Frank A. Marcos/LKB		10. PROGRAM ELEMENT, PROJECT, TASK AREA & WORK UNIT NUMBERS (16) 62101F 6690202 (17) 92	
14. MONITORING AGENCY NAME & ADDRESS (if different from Controlling Office) (12) 64p.		12. REPORT DATE (11) 31 August 1977	
		13. NUMBER OF PAGES 63	
		15. SECURITY CLASS. (of this report) Unclassified	
		15a. DECLASSIFICATION/DOWNGRADING SCHEDULE	
16. DISTRIBUTION STATEMENT (of this Report) Approved for public release; distribution unlimited.			
17. DISTRIBUTION STATEMENT (of the abstract entered in Block 20, if different from Report)			
18. SUPPLEMENTARY NOTES			
19. KEY WORDS (Continue on reverse side if necessary and identify by block number) Accelerometer Solar Radiation Pressure Measurement Acceleration Solar Radiation Electrostatic Accelerometer			
20. ABSTRACT (Continue on reverse side if necessary and identify by block number) This report describes analytical studies performed to optimize the measurement of solar radiation pressure on the NTS-3 satellite using a three axis electrostatic accelerometer.			

408855

JP

ACCESSION for	
NTIS	White Section <input checked="" type="checkbox"/>
DDC	Buff Section <input type="checkbox"/>
ORIGINATOR	<input type="checkbox"/>
JUSTIFICATION	
BY	
DISTRIBUTION/AVAILABILITY CODES	
Dist.	AVAIL. and/or SPECIAL
A	

INDEX

	<u>Page</u>
I ABSTRACT	1
II INTRODUCTION	1
III CONCLUSIONS	1
IV RECOMMENDATIONS	2
V SATELLITE ACCELERATION ENVIRONMENT	3
VI SATELLITE ACCELERATION MEASUREMENT	7
VII SYSTEM DESIGN CONFIGURATION	21
VIII DATA TRANSMISSION AND REDUCTION	50
APPENDIX A, MESA ACCELERATION ALGORITHM	53

FIGURES

<u>Number</u>	<u>Title</u>	<u>Page</u>
V-1	RESPONSE OF RIGID MASS NODE TO A STEP YAW TORQUE OF 0.04 FT-LB	4
VI-1	SYSTEM BLOCK DIAGRAM	8
VI-2	INSTRUMENT CASE MOUNTED IN CENTRIFUGE	10
VI-3	ANALYTICAL COORDINATE SYSTEM	11
VI-4	ELLIPTICAL CYLINDER	18
VI-5	FLARED PROOF MASS AND ELECTRODE CARRIER	18
VII-1	INPUT-DEPENDENT COUPLING FACTOR	22
VII-2	PROOF MASS AND ELECTRODE CONFIGURATION	26
VII-3	INSTRUMENT CASE MOUNTED IN CENTRIFUGE	27
VII-4	BLOCK DIAGRAM CONSTRAINTMENT LOOP	32
VII-5	RESOLUTION GRAPH	33
VII-6	TELEMETRY INTERFACE CIRCUIT	41
VII-7	BLOCK DIAGRAM GROUND SUPPORT EQUIPMENT (GSE)	48
VII-8	TYPICAL FUNCTIONAL TEST CONNECTIONS	49

Preceding Page BLANK - NOT FILMED

FIGURES (CONT)

<u>Number</u>	<u>Title</u>	<u>Page</u>
VIII-1	ACCELEROMETER SYSTEM DATA FLOW	52
A-1	FORCE VECTOR DIAGRAM	53

TABLE

<u>Number</u>	<u>Title</u>	<u>Page</u>
VI-1	VEHICLE ACCELERATION ERROR TERMS	13

I. ABSTRACT

This report describes analytical studies performed to optimize the measurement of solar radiation pressure on the NTS-3 satellite using a three axis electrostatic accelerometer.

II. INTRODUCTION

The study was conducted to define those characteristics of the satellite and accelerometer which will influence the measurement and determine its accuracy. This included definition of the NTS-3 acceleration levels, defining the accelerometer system performance requirements, defining the mechanical and electrical interface requirements, and establishing data transmissions and reduction constraints.

III. CONCLUSIONS

Based on currently available NTS-2 and NTS-3 data and the limited scope of this study, the following conclusions are drawn:

1. Measurement of the NTS acceleration due to solar pressure can be achieved with an accuracy of 1% or better by the proposed accelerometer system configuration.

2. Amplitude modulation of the solar radiation acceleration coupled with synchronous demodulation and filtering of the accelerometer output signal will provide the required discrimination between the signal and satellite generated noise.

3. Primary acceleration noise sources on the satellite are the gravity gradient stabilization system, the solar array drive mechanism, and the accelerometer proof mass constraint electronics.

4. On orbit calibration of the accelerometer scale factor should be provided to achieve the required accuracy.

IV. RECOMMENDATIONS

The following recommendations are made to achieve the desired 1% measurement accuracy consistent with the NTS-3 design, fabrication, test, and flight schedules.

1. NTS-2 flight data should be reviewed and the study effort updated to reflect spacecraft on-orbit performance.

2. Perform an evaluation of the possible impact of acceleration noise generated by the satellite momentum wheels.

3. Provide basic envelope, weight, and power estimates to NRL for consideration during the initial NTS-3 design phases.

4. NTS-3 design should provide for an on-center-of-gravity location for the accelerometer portion of the acceleration measurement system.

5. Consideration should be given to increasing the on-board storage capacity by a factor of 4 or data compression technique should be incorporated in the acceleration measuring system.

6. Development and design of the proposed acceleration measurement systems should be pursued consistent with the NTS-3 schedule.

V. SATELLITE ACCELERATION ENVIRONMENT

A. Satellite Rotation Rates and Angular Accelerations

The primary sources of satellite angular accelerations and velocities are the disturbing torques acting on the spacecraft due to solar pressure unbalance, magnetic torques, gravity gradient rod thermal bending, orbit eccentricity and solar array drive. The attitude and angular rate errors based on simulation runs described in reference 1 are given below.

Roll Attitude	0.15 degrees peak
Pitch Attitude	0.15 degrees peak
Pitch Rate	$1.22 \times 10^{-4} \sin \omega_0 t$ rad/sec
Roll Rate	$2.82 \times 10^{-5} \sin 2\omega_0 t$ rad/sec
Yaw Rate	$1.7 \times 10^{-4} \sin \omega_0 t$ rad/sec

$$\omega_0 = 1.45 \times 10^{-4} \text{ rad/sec}$$

The angular accelerations are derived from differentiation of angular rates since they are primarily sinusoidal at ω_0 and $2\omega_0$.

Pitch Acceleration	$1.77 \times 10^{-8} \cos \omega_0 t$ rad/sec ²
Roll Acceleration	$8.2 \times 10^{-9} \cos 2\omega_0 t$ rad/sec ²
Yaw Acceleration	$2.46 \times 10^{-8} \cos \omega_0 t$ rad/sec ²

B. Solar Array Drive

The solar array drive accelerations are based upon the dynamic analysis of the spacecraft (reference 2). The response of the equivalent rigid mass at the spacecraft c.g. is shown in Figure V-1.

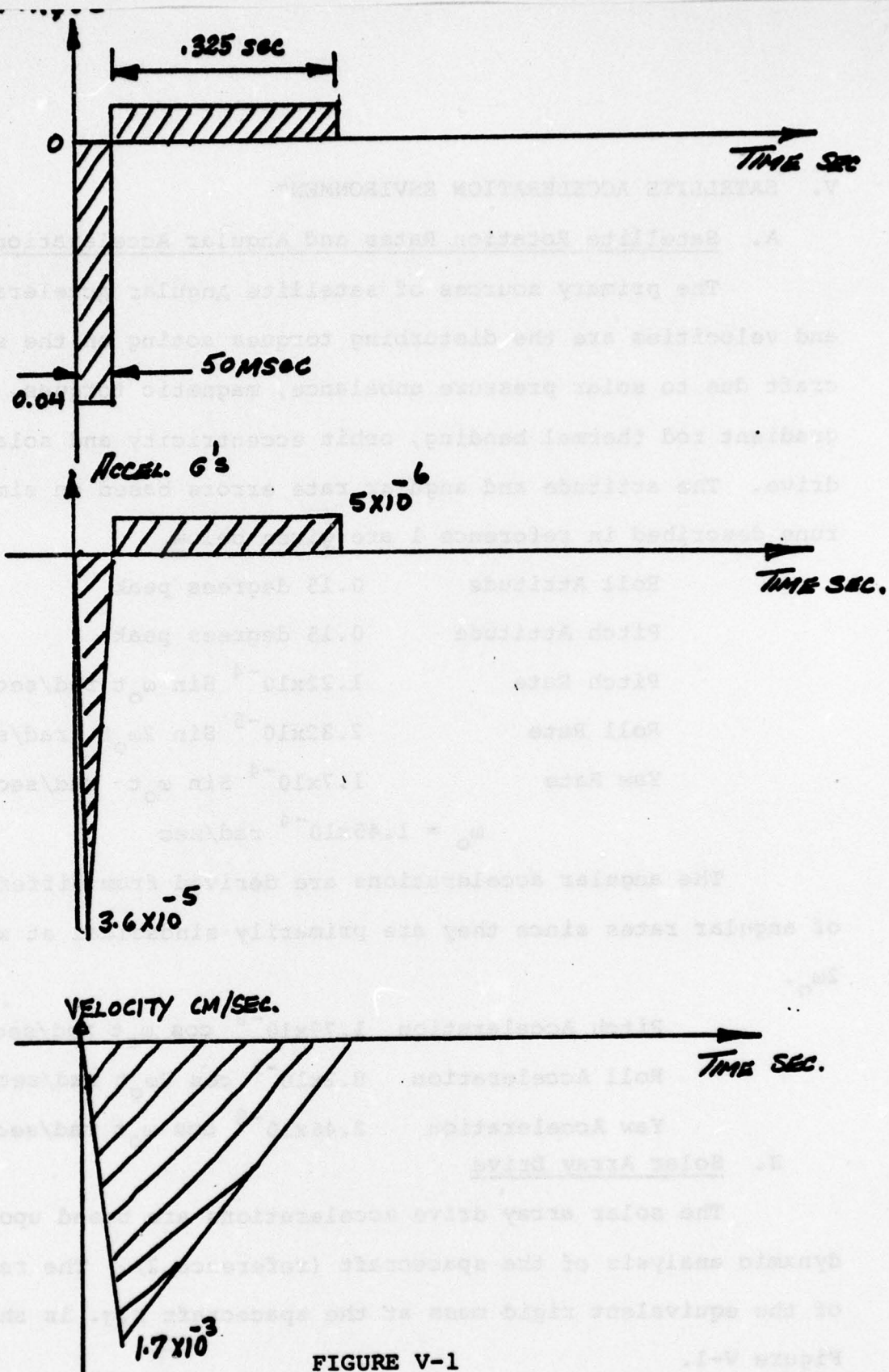


FIGURE V-1

RESPONSE OF RIGID MASS NODE TO A STEP YAW TORQUE OF 0.04 FT-LB

C. Vehicle Control and Structural Resonance

The data on vehicle control and structural resonance characteristics is based upon information obtained from reference

3. The open loop control system poles are as follows:

1) Pitch and Roll

Low freq pole @ 1.67 orbital freq = 2.44×10^{-4} rad/sec

Symmetrical Bending 0.0390 rad/sec

Assymetrical Bending 0.19 rad/sec (Yaw)

0.14 rad/sec (Roll)

2) Yaw (also coupled to Roll)

Low freq pole @ orbital freq = 1.46×10^{-4} rad/sec

Cantilever Mode 0.0398 rad/sec

The structural resonances are (reference 2)

1) Solar array natural freq 0.16 hz

2) Rod Bending Modes (hz) 0.019, 0.026, .366, 1.98,
2.0, 4.28

Since it is difficult to predict the acceleration levels in these modes, the rotation rate and MESA frequency response should be set below these frequencies to minimize noise at these frequencies.

D. Solar Pressure Acceleration

The expected solar pressure acceleration level is based upon data obtained from reference 4. The approximate acceleration levels are as follows:

$$A_{XCG} = -8 \cdot 10g^{-9} \text{ to } -9 \cdot 10g^{-9}$$

$$A_{YCG} = 3 \cdot 10g^{-11}$$

$$A_{ZCG} = -2 \cdot 10g^{-11} \text{ to } +5 \cdot 10g^{-9}$$

The calculations are based on a model consisting of 11 flat surfaces, upper and lower cylinders of the gravity booms and the upper and lower spheres of the gravity booms. The antennas and magnetometer were not included in the model. The diffuse and specular reflection coefficient values used in the model were based on analytical data, not on satellite test data.

VI. SATELLITE ACCELERATION MEASUREMENT

A. Measurement Requirement

The 3-axis measurement of the satellite solar pressure acceleration levels of approximately 10^{-8} to $10^{-11}g$ is difficult because of other accelerations due to:

1. Vehicle dynamic control
2. Solar array drive
3. Structural resonances

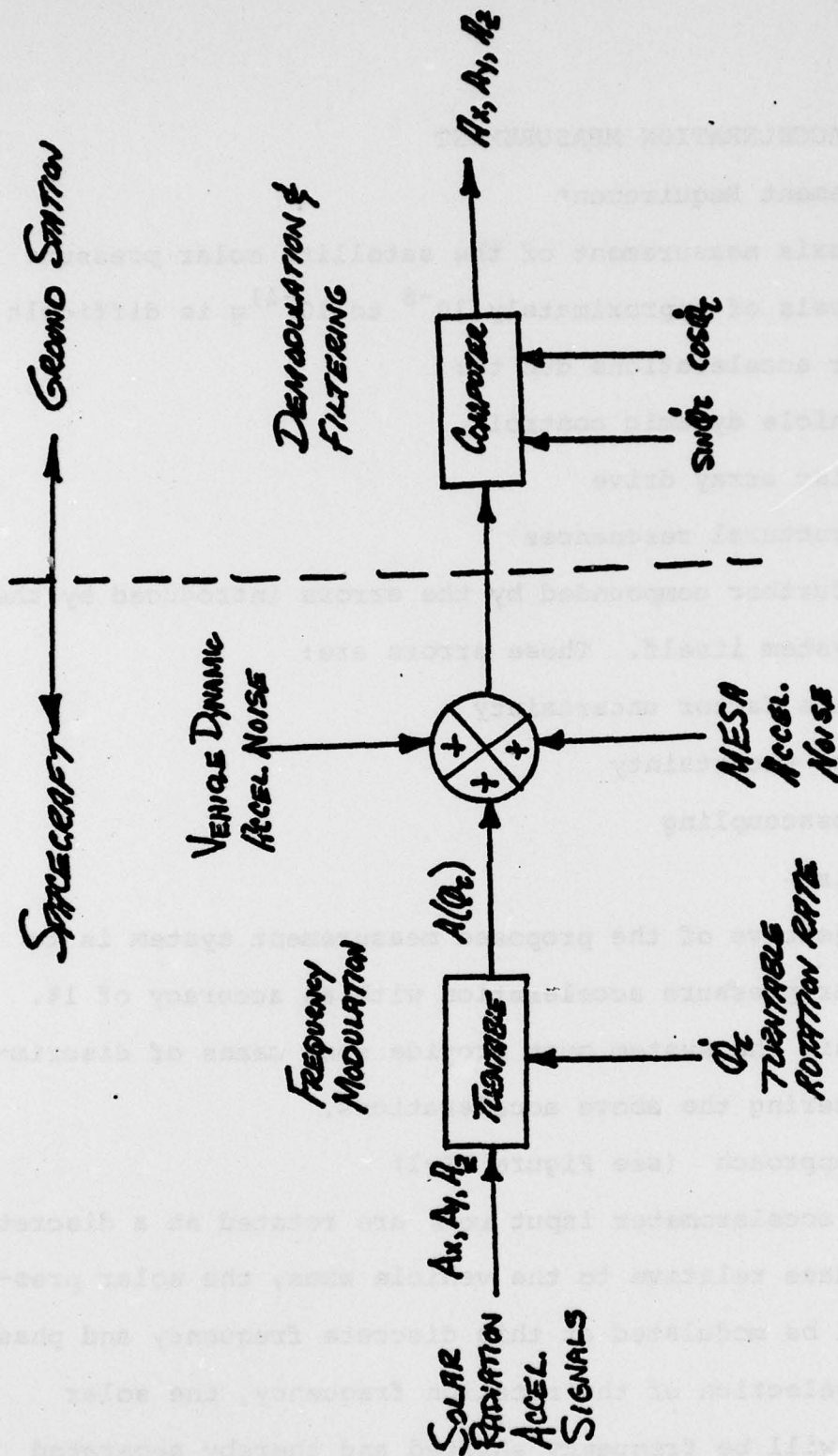
It is further compounded by the errors introduced by the accelerometer system itself. These errors are:

1. Scale factor uncertainty
2. Bias uncertainty
3. Crosscoupling
4. Noise

The objective of the proposed measurement system is to measure the solar pressure acceleration with an accuracy of 1%. To accomplish this the system must provide some means of discriminating and filtering the above accelerations.

B. Basic Approach (see Figure VI-1)

If the accelerometer input axes are rotated at a discrete frequency and phase relative to the vehicle axes, the solar pressure signal will be modulated at this discrete frequency and phase. By appropriate selection of the rotation frequency, the solar pressure signal will be frequency shifted and thereby separated from other vehicle accelerations and accelerometer errors. This



SYSTEM BLOCK DIAGRAM

FIGURE VI-1

is accomplished by mounting the accelerometer on a rotating table as shown in Figure VI-2.

The centripetal acceleration due to the table rotation will also introduce a known input acceleration which is used to calibrate the accelerometer scale factor.

The X, Y and Z outputs of the accelerometer are synchronously demodulated and filtered.

C. Analysis of Measured Accelerations

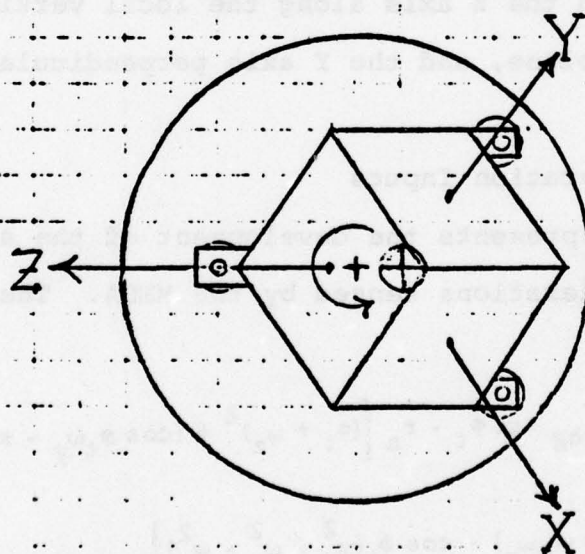
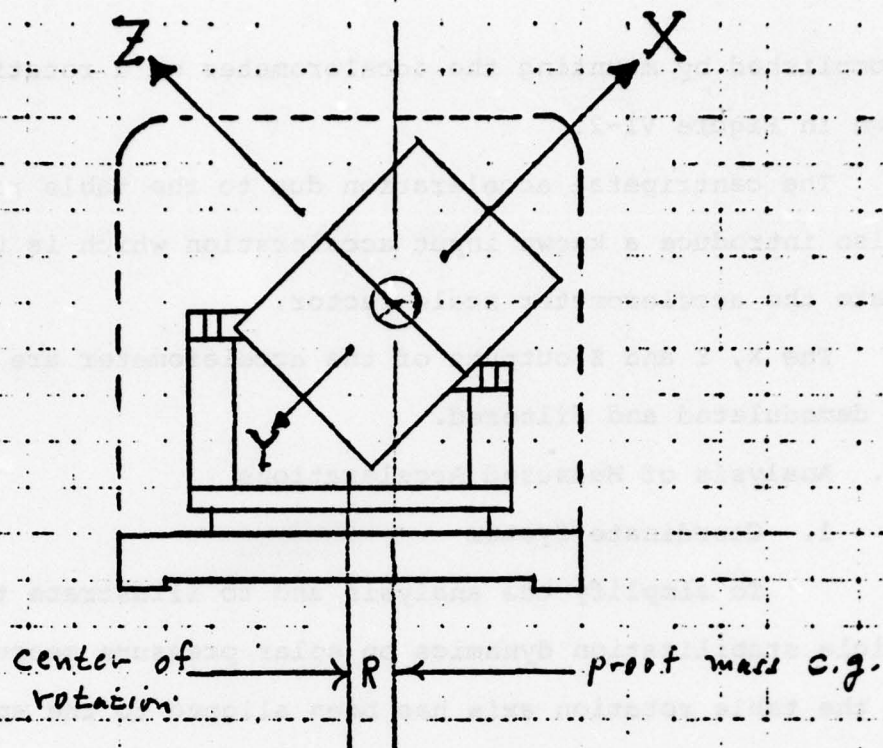
1. Coordinate System

To simplify the analysis and to illustrate the effect of vehicle stabilization dynamics on solar pressure measurement error, the table rotation axis has been aligned to the spacecraft Z axis as shown in Figure VI-3. The coordinate system shown is a right handed system with the Z axis along the local vertical, the X-Z plane in the orbit plane, and the Y axis perpendicular to the orbit plane.

2. MESA Acceleration Inputs

Appendix A presents the development of the algorithm for the input axis accelerations sensed by the MESA. The final results are:

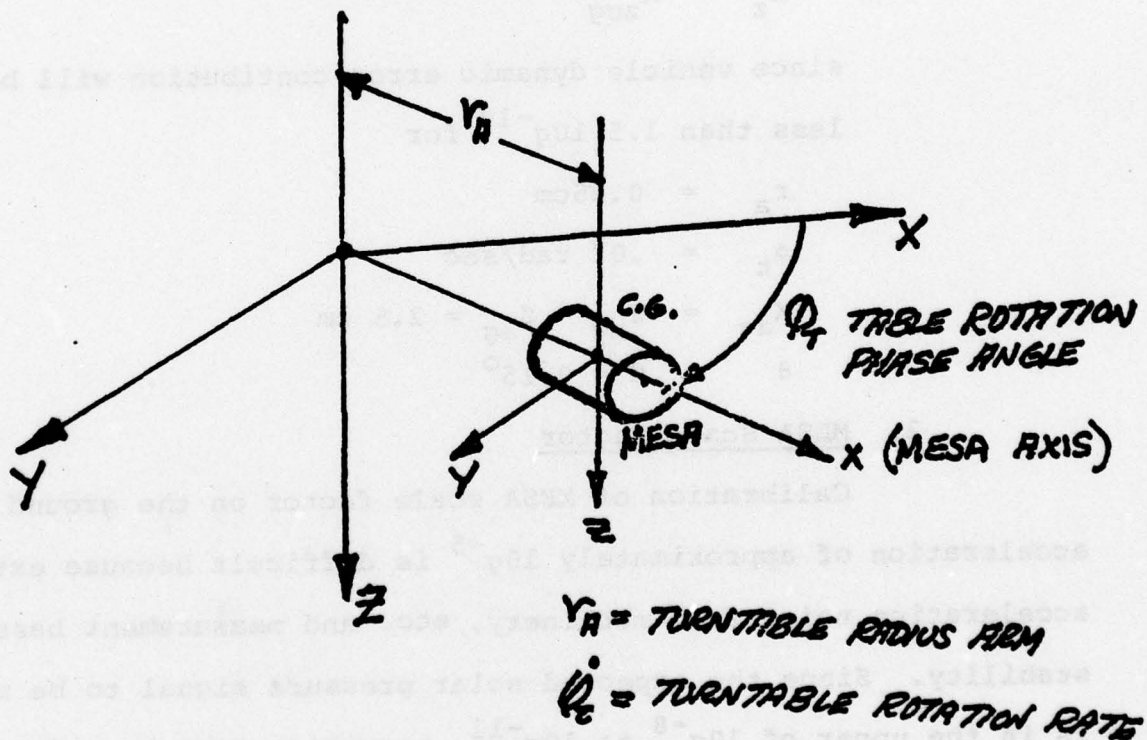
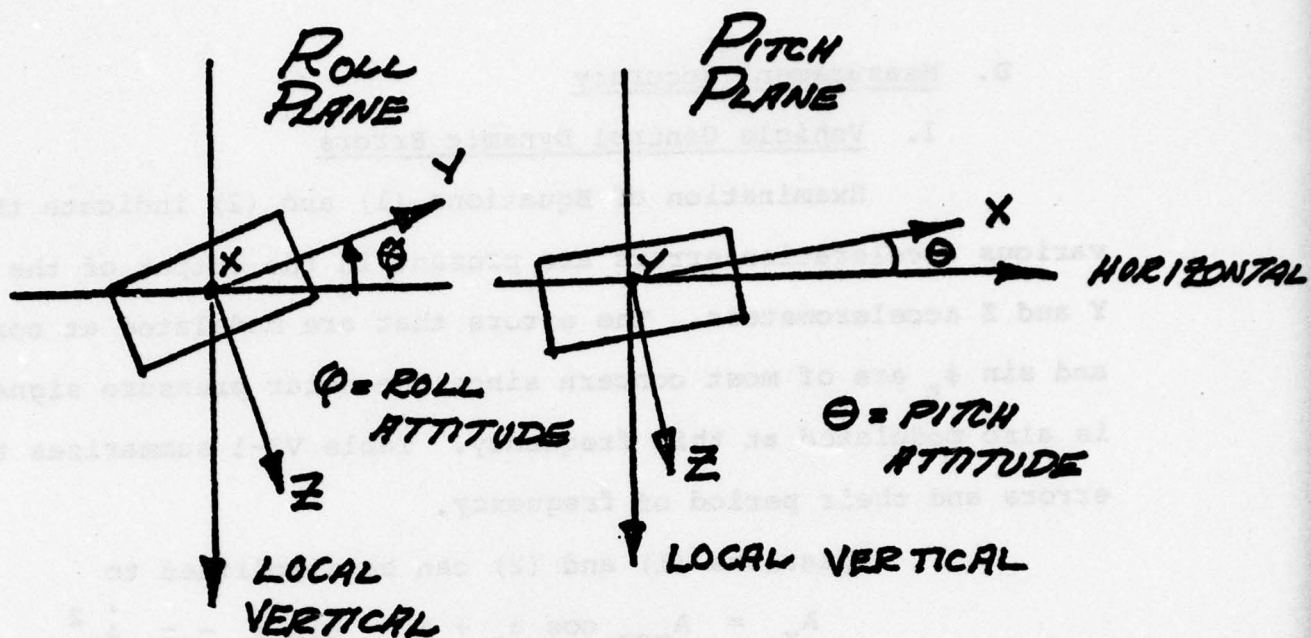
$$\begin{aligned}
 A_x = & A_{xcg} \cos \phi_t + A_{ycg} \sin \phi_t - r_a \left[(\dot{\phi}_t + \omega_z)^2 + (\cos \phi_t \omega_y - \sin \phi_t \omega_x)^2 - \omega_o^2 \right] \\
 & + X_{ag} \left[\sin \phi_t (\dot{\omega}_z + \omega_x \omega_y) - \cos \phi_t (\omega_y^2 + \omega_z^2 - \omega_o^2) \right] \\
 & + Y_{ag} \left[\cos \phi_t (-\dot{\omega}_z + \omega_x \omega_y) - \sin \phi_t (\omega_x^2 + \omega_z^2 - \omega_o^2) \right] \\
 & + Z_{ag} \left[\cos \phi_t (\omega_x \omega_z + \dot{\omega}_y + 3\omega_o^2 \theta) - \sin \phi_t (\dot{\omega}_x - \omega_y \omega_z + 3\omega_o^2 \varphi) \right]
 \end{aligned} \tag{1}$$



$$A_{(X,Y,Z)} = 0.7071 \cdot \omega^2 R$$

Instrument Case Mounted in Centrifuge

FIGURE VI-2



ANALYTICAL COORDINATE SYSTEM

FIGURE VI-3

D. Measurement Accuracy

1. Vehicle Control Dynamic Errors

Examination of Equations (1) and (2) indicate that various acceleration errors are present in the output of the X, Y and Z accelerometers. The errors that are modulated at $\cos \phi_t$ and $\sin \phi_t$ are of most concern since the solar pressure signal is also modulated at this frequency. Table VI-1 summarizes these errors and their period of frequency.

Equations (1) and (2) can be simplified to

$$A_x = A_{xcg} \cos \phi_t + A_{ycg} \sin \phi_t - r_a \dot{\phi}_t^2$$

$$A_y = A_{xcg} \sin \phi_t + A_{ycg} \cos \phi_t - r_a \dot{\phi}_t^2$$

$$A_z = A_{zcg}$$

since vehicle dynamic error contribution will be less than $1.5 \cdot 10g^{-10}$ for

$$r_a = 0.25 \text{ cm}$$

$$\phi_t = .02 \text{ rad/sec}$$

$$X_{ag} = Y_{ag} = Z_{ag} = 2.5 \text{ cm}$$

$$\theta = \phi = 0.15^\circ$$

2. MESA Scale Factor

Calibration of MESA scale factor on the ground below acceleration of approximately $10g^{-5}$ is difficult because external acceleration noise from machinery, etc. and measurement base tilt stability. Since the expected solar pressure signal to be measured is in the upper of $10g^{-8}$ to $10g^{-11}$, provision must be made to calibrate MESA scale factor in orbit.

TABLE VI-1. VEHICLE ACCELERATION ERROR TERMS

($r_a = 0.25$ cm, $\dot{\phi}_t = 0.02$ rad/sec, $x_{ag} = y_{ag} = z_{ag} = 2.5$ cm, $\theta = \phi = .15^\circ$)

Error Term	Amplitude $\hat{\phi}$ (g's)			
	D.C.	ω_o	$2\omega_o$	ϕ
$r_a (\dot{\phi}_t + \omega_z)^2$	10^{-7}	$1.75 \cdot 10^{-9}$	$2.5 \cdot 10^{-12}$	-
$r_a [(\cos \phi_t \omega_y - \sin \phi_t \omega_x)^2 - \omega_o^2]$	$5 \cdot 10^{-12}$	$3.6 \cdot 10^{-13}$	$3.6 \cdot 10^{-13}$	-
$x_{ag} [\sin \phi_z (\dot{\omega}_z + \omega_x \omega_y) - \cos \phi_z (\omega_y^2 + \omega_z^2 - \omega_o^2)] - 6.2 \cdot 10^{-11}$	-	$6.2 \cdot 10^{-11}$		$6.2 \cdot 10^{-11}$
$y_{ag} [\cos \phi_t (\omega_x \omega_y - \dot{\omega}_z) - \sin \phi_t (\omega_x^2 + \omega_z^2 - \omega_o^2)] - 6.2 \cdot 10^{-11}$	-	$6.2 \cdot 10^{-11}$		$6.2 \cdot 10^{-11}$
$z_{ag} [\cos \phi_t (\omega_x \dot{\omega}_z + \omega_y^2 + 3\omega_o^2) - \sin \phi_t (\dot{\omega}_x - \omega_y \omega_z + 3\omega_o^2 \phi)] -$				$4.2 \cdot 10^{-13}$
$r_a [\cos \phi_t (\dot{\omega}_y + \omega_o^2 3\theta + 2\omega_x \dot{\phi}_t - \omega_x \omega_z)]$	-	-	$3 \cdot 10^{-10}$	-
$r_a [\sin \phi_t (2\omega_y \dot{\phi}_t + \omega_y \omega_z + \dot{\omega}_x + \omega_o^2 3\phi)]$	-	-	$1.5 \cdot 10^{-10}$	-
$x_{ag} [\dot{\omega}_y + \omega_o^2 3\theta - \omega_x \omega_z]$	$3.8 \cdot 10^{-11}$	$4.5 \cdot 10^{-12}$	$1.2 \cdot 10^{-11}$	-

Typical turntable centripetal accelerations for various rates and radius arms are shown below:

$\gamma(\text{sec})$	$\dot{\phi}_t(\text{rad/sec})$	Centripetal Accel (ug's)	
		$r = 0.25 \text{ cm}$	$r = 1.25 \text{ cm}$
100	.0628	.9	4.5
200	.0314	.228	1.14
300	.0209	.102	.510
400	.0157	.057	.285
500	.0125	.036	.18

The selection of the turntable rate is based on the requirement to minimize vehicle structural resonance and MESA noise as well as to provide a $10g^{-7}$ calibration signal and an adequate number of data points each orbit.

Based upon the above factors, a rotation rate of approximately 300 seconds is recommended. The steady state error introduced by table speed variations $\Delta\dot{\phi}_t$ is given by

$$\frac{\Delta a}{a} = \frac{1}{2} \left(\frac{\Delta\dot{\phi}_t}{\dot{\phi}_t} \right)^2$$

$$\text{For } \frac{\Delta a}{a} < 1\% \quad \frac{\Delta\dot{\phi}_t}{\dot{\phi}_t} < 1.4\%$$

The error introduced by radius arm uncertainty is given by

$$\frac{\Delta a}{a} = \frac{\Delta r_a}{r_a}$$

$$\text{For } \frac{\Delta a}{a} < 1\%, \quad \frac{\Delta r_a}{r_a} < 1\% \text{ or } .0025 \text{ cm}$$

$$r_a = 0.25 \text{ cm and } .0125 \text{ cm for } r_a = 1.25 \text{ cm}$$

The error due to MESA scale factor temperature sensitivity is typically $0.05\%/^{\circ}\text{C}$ which will result in an error in acceleration measurement of $\pm 0.5\%$ over an operating temperature range at $20^{\circ}\text{C} \pm 10^{\circ}\text{C}$. This may be reduced to 0.05% by using a temperature monitor or by inflight calibration.

The proposed scale factor error budget is summarized below.

<u>Error Source</u>	<u>% S.F. Error</u>
1. Turntable Rate $\frac{1}{2} \left(\frac{\Delta \dot{\phi}_t}{\dot{\phi}_t} \right)$	
For $\frac{\Delta \dot{\phi}_t}{\dot{\phi}_t} = .2\%$	0.1
2. Radius Arm $\frac{\Delta r_a}{r_a} = 0.5\%$	<u>0.5</u>
	RMS Error 0.51%

3. MESA Bias Uncertainty

One of the major advantages of the approach at frequency modulation of the solar pressure acceleration is that it eliminates the steady state or DC MESA bias error. It is desirable to minimize the nominal bias so that it is a small percent of the full scale range. In this case the nominal bias should be limited to $10g^{-8}$ for MESA suspension levels of $10g^{-6}$.

4. MESA Noise

Noise is generated from random molecular motion of gas molecules (thermal or Brownian motion) and constraint electronics. The noise error is given by

$$\bar{a}_n = \sqrt{\int_{f_1}^{f_2} P(f) df}$$

where $P(f)$ = noise power spectral density g^2/hz

f_2, f_1 = system measurement bandwidth

The amplitude of the power spectrum and the equivalent noise error are shown below for $f_2 = \frac{1}{300.2}$ hz and $f_1 = \frac{1}{300}$ hz. This corresponds to a table rotation period of 300 seconds and demodulator filter of 10 seconds.

\bar{a}_n (g rms)	$P(f)$ ($\mu g^2/hz$)
1.4×10^{-10}	.01
1×10^{-10}	.005
3×10^{-11}	.001

The MESA power spectral density for the present configuration is higher in the cross (X and Y) axes than in the longitudinal Z axis because of the higher loop gain and damping in the cross axis. The cube shaped proof mass will have the same PSD in all axes and will be the same as the present Z axis. The present MESA PSD are shown below. The X and Y axes performance is marginal.

Axis	$P(f) \text{ ug}^2/\text{hz}$	$\bar{a}_n (g^2 \text{ rms})$
Z	.0002	2×10^{-11}
X, Y	.025	2.2×10^{-10}

5. Cross Coupling

Accelerations present in the axis (whether steady state or random) will crosscouple into the other two axes depending on the proof mass geometry. To minimize crosscoupling errors, the forces acting on the proof mass should be orthogonal to one another. This non-orthogonality coupled with geometric imperfections introduces static and dynamic/crosscoupling errors.

In the case of the present cylindrical proof mass with the circular flange shown in Figures VI-4 and VI-5, cross-coupling between X and Y axes is very large because of the cylindrical shape. It is lower between the X, Y and Z axes due to the orthogonality of the flange and cylinder. Distortion of the cylinder (flared or elliptical) results in crosscoupling errors which are a function of that angular rotation about the Z axis, this motion being unconstrained.

Elliptical Cylinder

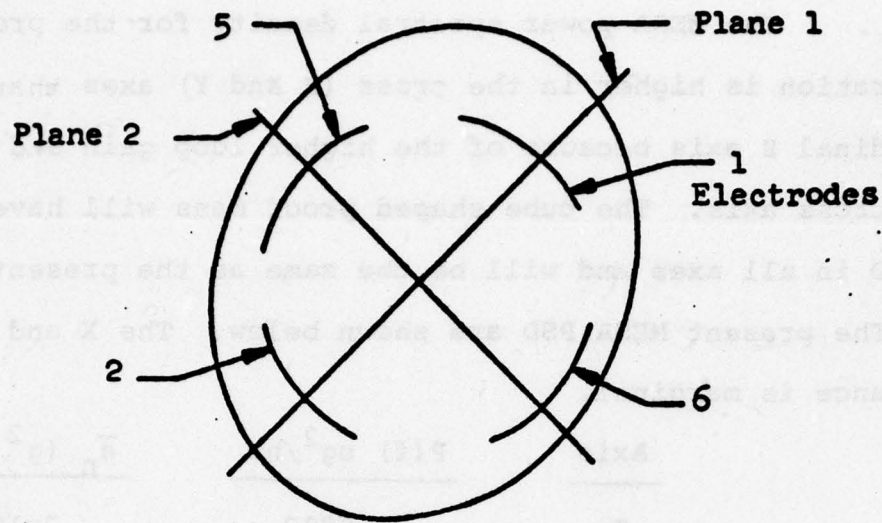
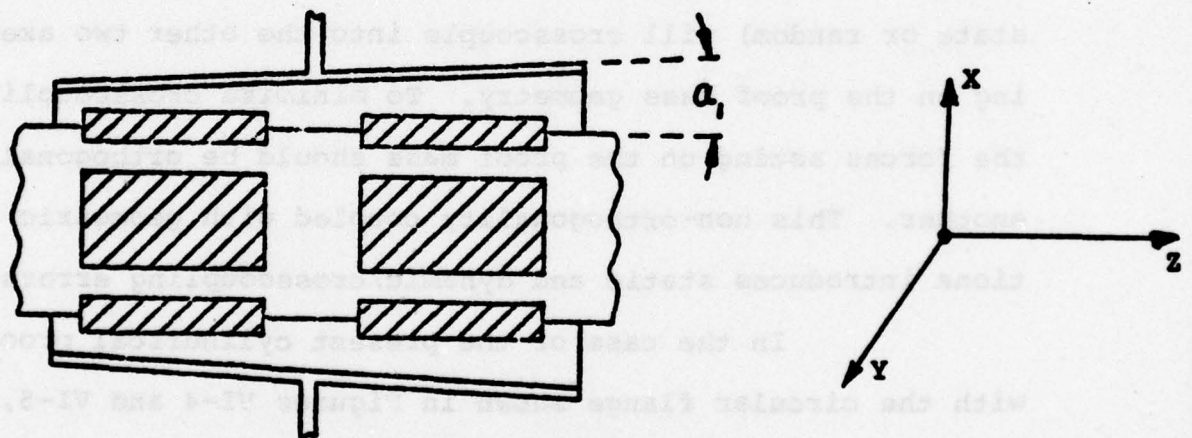


FIGURE VI-4



FLARED PROOF MASS AND ELECTRODE CARRIER

FIGURE VI-5

In order to minimize crosscoupling between the X and Y axes, the loop gain must be very high which results in higher electronic noise in these axes.

<u>Proof Mass Configuration</u>		<u>Non g-Sensitive g/g Scaling</u>	<u>g-Sensitive g/g Scaling/g input</u>
1. Cylindrical Float and Flange Z		10^{-4}	10^{-4}
	X, Y	10^{-2}	10^{-4}
2. Cube	X,Y,Z	3×10^{-5}	10^{-5}

For a constraint or scaling level in each axis of $10g^{-6}$, the resulting errors are as follows.

<u>Proof Mass Configuration</u>		<u>Non g-Sensitive</u>	<u>g-Sensitive g/g input</u>
1. Cylindrical Float and Flange Z		10^{-10}	10^{-10}
	X, Y	10^{-8}	10^{-10}
2. Cube	X,Y,Z	3×10^{-11}	10^{-11}

REFERENCES

1. Final Report on the Attitude Control Analysis of NTS-2, Report No. 75SDS4247, October 24, 1975, General Electric Co.
2. Independent Stability and Control Analysis of Navigational Development Satellite for GPS. Interim Report Sept., October 1976, Report No. F0360-19, Honeywell Inc.
3. Final Report Analysis of Interaction Between the Spacecraft Flexible Structure and the Attitude Control System for NTS-2 Report No. 76SDS4215, March 25, 1976, General Electric Co.
4. Personal Communication, Cary Chen, NSWC

VII. SYSTEM DESIGN CONFIGURATIONS

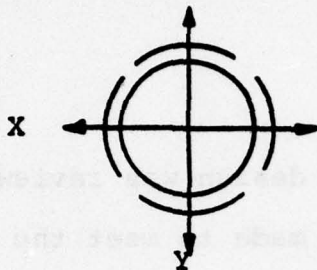
A. Instrument Mechanical Design

The current instrument mechanical design was reviewed to determine what, if any, changes should be made to meet the NTS-3 application requirements. The signal levels expected are somewhat lower than previous applications. This will require a substantial reduction of internal electronic noise levels.

Since the constraint loop gain and bandwidth influence the noise levels, the mechanical design was reviewed to determine its influence on these parameters.

The major requirement for high loop gain is to reduce proof mass motion over the expected input acceleration levels. The current flanged cylinder proof mass requires extremely high gain loops in the two axes which are normal to the cylinder axis. This is a direct result of electrode geometry (curved surfaces) which generate gross coupling forces when deflected from its normally centered or null position. This effect is illustrated in Figure VII-1.

Centered Proof Mass
No Acceleration Input



Proof Mass Displaced by
X Axis Acceleration Input

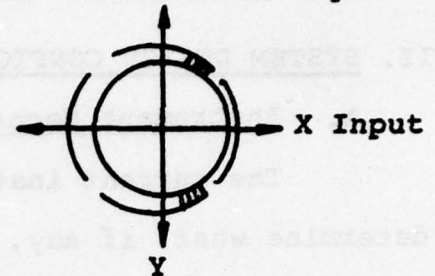


Figure VII-1. Input-Dependent Coupling Factor

Displacing the proof mass in the X axis causes a decreased gap on one side of the Y axis electrodes. This causes the Y axis electrode voltages to force the proof mass still further to the right as illustrated in Figure VII-1. To compensate for this additional force, the X axis loop must now develop an additional constraining force increment which is not the direct result of input acceleration.

To eliminate this effect and hence the high loop gain and resultant noise, the electrodes and proof mass should be flat and normal to each other in the two axes.

To achieve this requires the use of a different geometry proof mass.

In an ideal three axis accelerometer, the proof mass should be completely symmetrical in all three axes. The two most practical shapes which come to mind and meet this requirement are variations of the sphere and cube. The sphere was ruled out since it would not solve the problem of cross coupling due to curved surfaces as shown in Figure VII-1. In fact it would add this problem to the remaining axis which was a flat surface in the flanged cylinder. Fabrication of a hollow sphere has been perfected to some degree in the design of gyros, and would probably not be a major reason for not considering it. The effect of dimensional tolerances could be eliminated by rotation of the sphere but this would further complicate the electronics and still not solve the cross coupling factor.

The cube will satisfy the symmetry requirement as well as providing three orthogonal flat surfaces in each axis.



Two variations of the cube shape were considered. One is simply a hollow cube, the other is a cruciform or three intersecting flat planes. The later was ruled out because of high

fabrication costs and the need for 24 electrodes facing the proof mass versus 12 for the cube.

A preliminary drawing of the hollow cube was prepared and submitted to a qualified supplier for the purpose of fabricating a feasibility unit. The original drawing called for a one inch hollow cube with .010 inch wall thickness. This closely simulated the available forcing area and weight of the flanged cylinder.

A study of fabrication techniques by the supplier showed that the flatness, perpendicularity, and parallelism requirements of the drawing could not be met with reasonable yield and hence costs.

Further analyses showed that reducing the size from 1 inch to 1/2 inch and increasing the wall thickness to .015 would probably meet the accuracy requirements of the drawing with a reasonable yield. A prototype unit was fabricated and measurements yielded the following data:

<u>Characteristic</u>	<u>Drawing</u>	<u>Measured</u>
 flatness all 6 surfaces	.0001"	.00005"
 perpendicularity adjacent	.0001"	.00005"
// parallelism opposite surfaces	.0001"	.00005"
Weight	.600 grams	.563 grams

Based on this data, the fabrication of a hollow cube proof mass appears feasible.

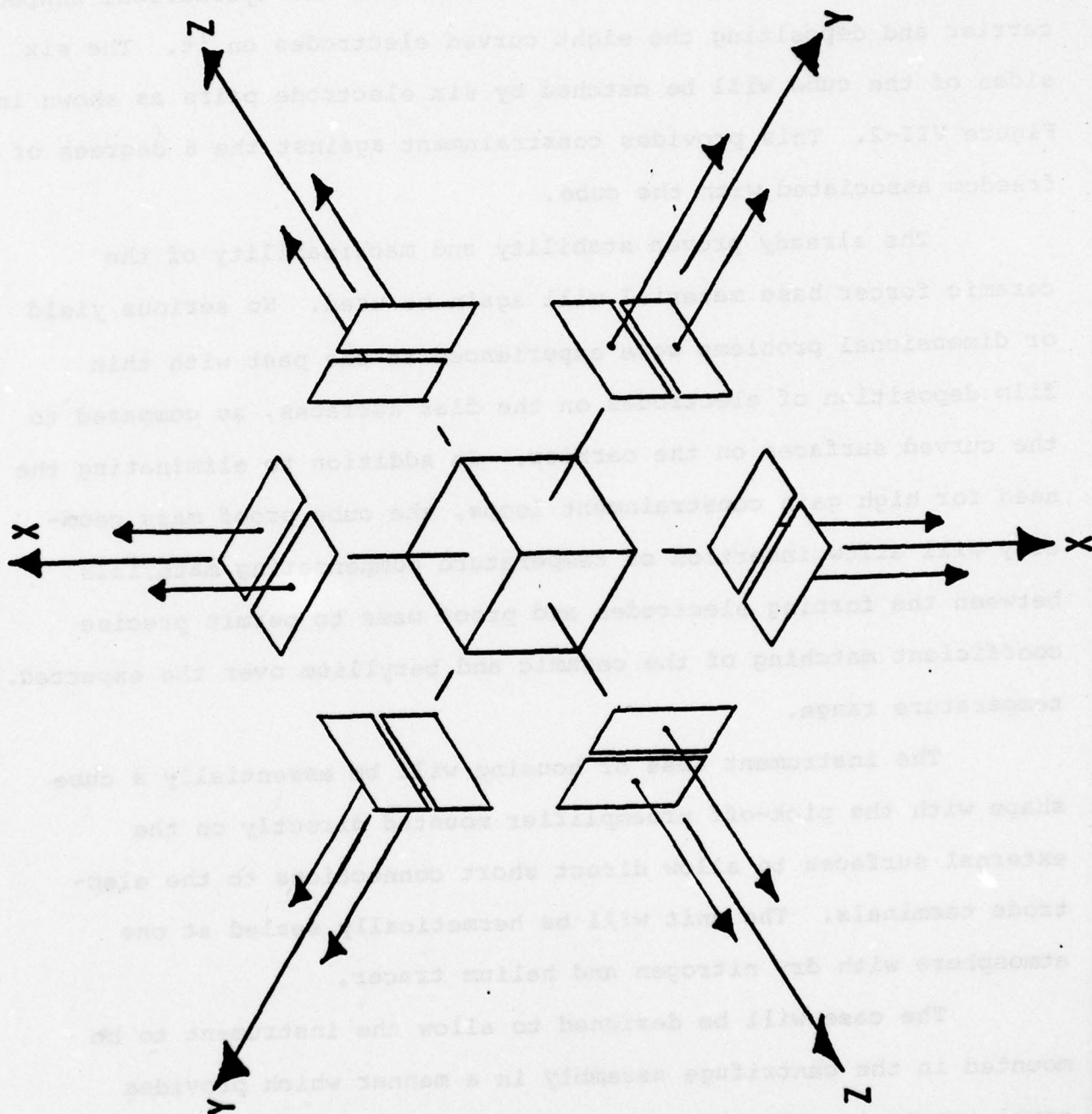
Other mechanical design features of the instrument were also reviewed with the goal of increasing performance. The use of a cube proof mass also removes the need to fabricate the cylindrical shaped carrier and depositing the eight curved electrodes on it. The six sides of the cube will be matched by six electrode pairs as shown in Figure VII-2. This provides constraint against the 6 degrees of freedom associated with the cube.

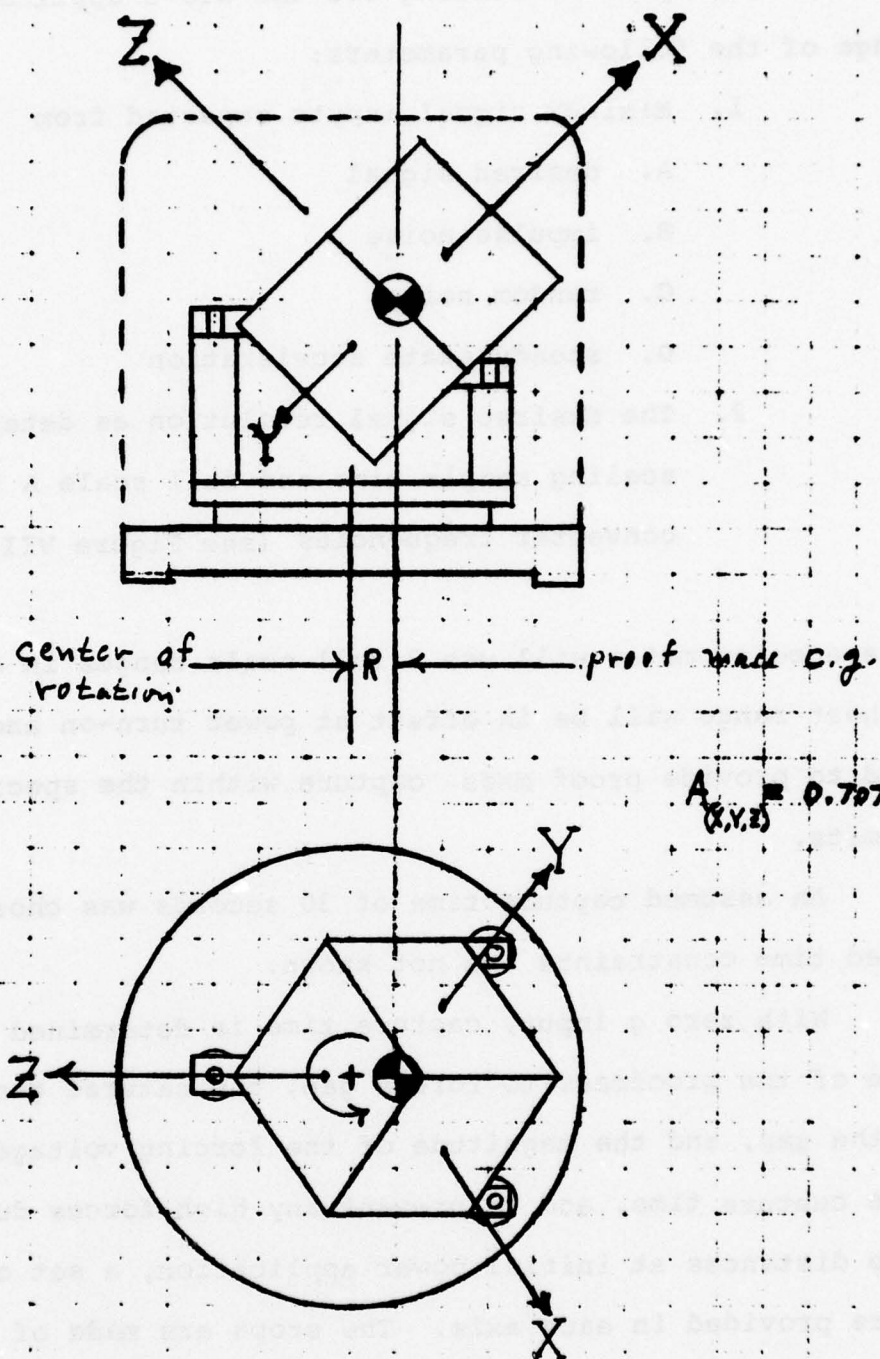
The already proven stability and machinability of the ceramic forcer base material will again be used. No serious yield or dimensional problems were experienced in the past with thin film deposition of electrodes on the flat surfaces, as compared to the curved surfaces on the carrier. In addition to eliminating the need for high gain constraint loops, the cube proof mass geometry will allow insertion of temperature compensating materials between the forcing electrodes and proof mass to permit precise coefficient matching of the ceramic and beryllium over the expected temperature range.

The instrument case or housing will be essentially a cube shape with the pick-off preamplifier mounted directly on the external surfaces to allow direct short connections to the electrode terminals. The unit will be hermetically sealed at one atmosphere with dry nitrogen and helium tracer.

The case will be designed to allow the instrument to be mounted in the centrifuge assembly in a manner which provides equal inputs in all axes. A simplified diagram of the case mounting is shown in Figure VII-3. This arrangement places all three axes at 45° with respect to force vector resulting from rotation of the centrifuge.

PROOF MASS AND ELECTRODE CONFIGURATION





Instrument Case Mounted in Centrifuge

Figure VII-3

B . Scaling and Frequency Response

To optimize scaling for the NTS-3 application requires knowledge of the following parameters:

1. Maximum signal inputs expected from
 - A. desired signal
 - B. impulse noise
 - C. random noise
 - D. steady state acceleration
2. The desired signal resolution as determined by scaling sample time and full scale A to D converter frequencies (see Figure VII-2)

The accelerometer will use 3 full scale ranges in each axis. The highest range will be in effect at power turn-on and will be designed to provide proof mass capture within the specified time limits.

An assumed capture time of 30 seconds was chosen since specified time constraints are not known.

With zero g input, capture time is determined by the distance of the proofmass to forces gap, the natural gas damping within the gap, and the magnitude of the forcing voltage. To minimize capture time, and to prevent any high forces due to near zero gap distances at initial power application, a set of mechanical stops are provided in each axis. The stops are made of either epoxy or ruby to provide electrical insulation and are set in the center of each forcer electrode pair. They normally limit the proofmass motion to one half the gap width.

Using full scale constraint values of 10^{-4} , 10^{-5} and 10^{-6} g appears reasonable for this application. The 10^{-4} scale would be used for capture and also during ground testing when one axis is constrained at 1 g. This range would also be used during measurement of R on the centrifuge.

The 10^{-6} would be used during all in orbit measurements of solar pressure. The 10^{-5} would serve as an intermediate range which would act as an overrange, if for any reason the $\pm 10^{-6}$ input limits were exceeded.

Changing scales on all three axes will be accomplished by an autorange circuit which has been developed and flight proven on previous missions. The autorange will be in effect at all times unless overridden by a range command.

In normal operation, the autorange will keep all three axes on 10^{-4} from power turn-on until proofmass capture is attained. It will then switch all three axes to 10^{-5} and then to 10^{-6} providing the input limits do not exceed either of these values.

The up and down scaling response times may be varied from 0.1 seconds to 10 seconds depending on the rate and rise time of any accelerations due to impulse noise and thrusters.

Longer times will prevent unwanted changes due to noise, while the shorter times will cause rapid scaling changes if desired.

Frequency response of the constraint loops will also be optimized. The response is determined by the frequency content of the measured signal, noise generated within the constraint loop electronics, spurious acceleration inputs from other sources on board the satellite, and signal modulation rate of the centrifuge.

To maximize the signal to noise ratio, the bandwidth should be only sufficient to cover the highest signal frequency expected without attenuation. Under these conditions it would be ideal if all noise sources would be higher in frequency content by several orders of magnitude.

The frequency response can be controlled at a number of points within and outside of the constraint loop. The loop response will be determined by scaling, gain and the need for sufficient damping to prevent overshoot or ringing within the loop under noisy or impulse inputs.

C. Data Output

The acceleration signal originates as a bipolar analog voltage at a point in the constraint loop just prior to amplification before being applied to the forcing electrodes. The levels at this point are normalized to ± 10 v dc representing \pm full scale output on all ranges. Figure VII-4 is a simplified block diagram of one constraint loop.

The resolution is determined by sample time, full scale A/D conversion frequency, and full scale constraint loop capability. The relationship between these variables is shown in Figure VII-5.

The example shown illustrates typical values which could be used in the NTS-3 application.

Example:

Full scale constraint capability = $\pm 10^{-4}$ g

Full scale A/D conversion = ± 10 kHz

Sample time = 100 seconds

For these values the signal resolution in terms of 1 bit change per sample period would be 10^{-10} g.

The bidirectional counter capacity is also shown. The example would require 20 bits storage per sample period.

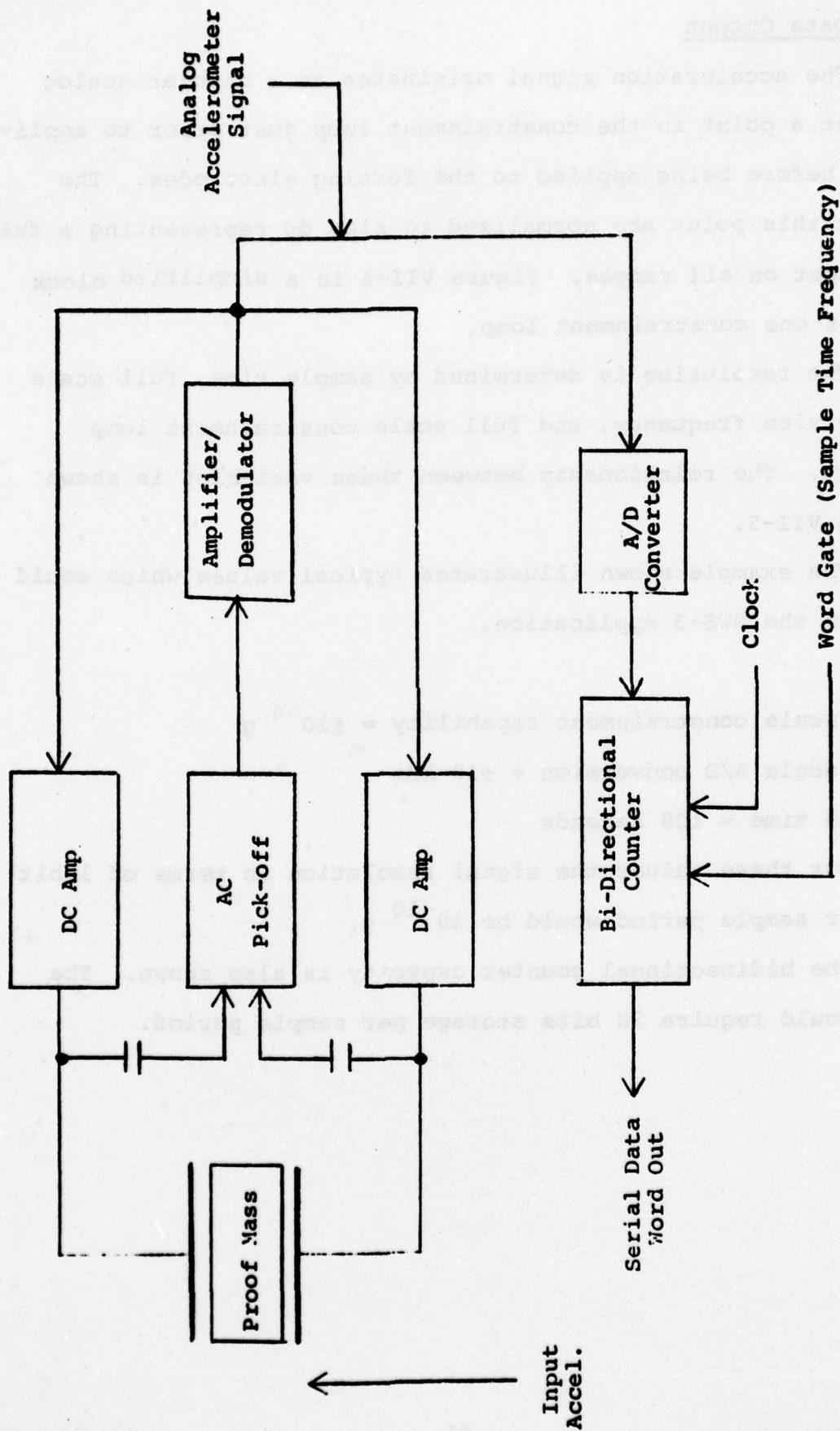


Figure VII-4. Block Diagram Constraint Loop

±Full Scale

Resolution 1 bit change per sample period

10^{-4}	10^{-10}	10^{-9}	10^{-8}
10^{-5}	10^{-11}	10^{-10}	10^{-9}
10^{-6}	10^{-12}	10^{-11}	10^{-10}

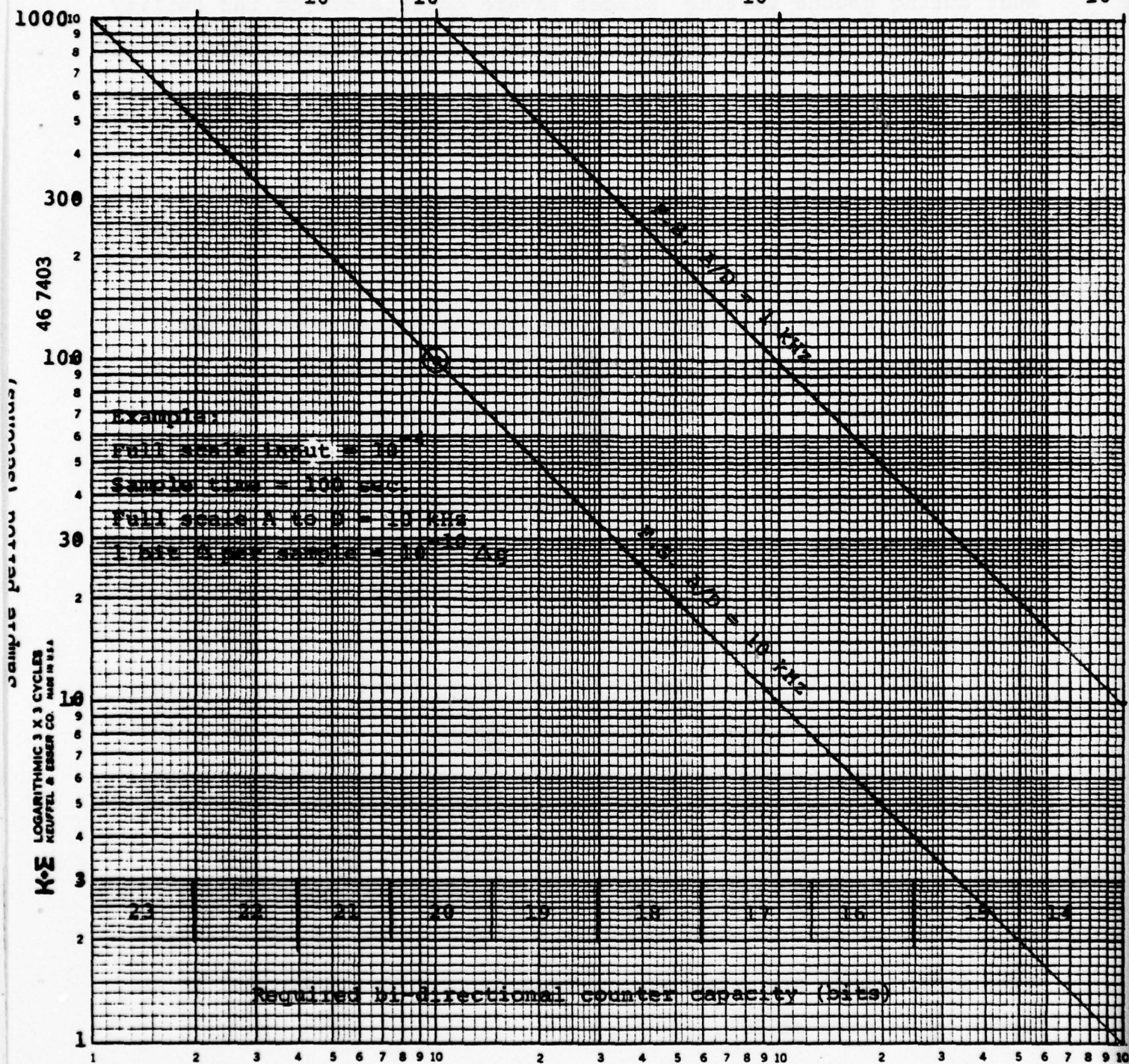


Figure VII-5. Resolution Graph

D. In-Flight Calibration of Scale Factor

The requirement to suspend the proof mass in a 1G environment during ground testing places severe constraints on the ability to measure scale factor accurately with full scale ranges of 10^{-5} or below.

Test base motion induced by building resonances and other made made disturbances will at times cause peak to peak input signals in excess of 10^{-4} g's. Predominant frequencies associated with this motion are 15, 30 and 60 Hz.

The normal instrument damping is sufficient to keep the constraint loops from saturating under these inputs when scaling is kept above 10^{-5} g. In actual practice the analog loops are normally set to have a constraint capability 10 to 20% greater than the full scale pulse rate of the output analog to digital converter. The test inputs are then limited to levels that do not allow the noise peaks to cause A to D converter saturation.

Full scale input limits of 10^{-6} g or lower are anticipated for the NTS-3 application. This makes accurate scale factor determination during ground test impossible unless new facilities with extremely low test base motions are made available.

Another reason for in flight calibration is that scale factor temperature coefficients need not be determined. The measurement of these coefficients are costly. The number of temperatures used during test are based on in orbit predictions which may be in error by as much as 25%.

Temperature control of the systems would eliminate most of the errors caused by temperature effects. In nearly all applications, heater power has not been available for this purpose.

Any unknown effects on scale factor as the result of applying lg to one axis during ground test are also eliminated as an error source. In flight calibration using a centrifuge is a proven technique and offers several unique advantages.

It provides a known input acceleration which can readily be changed upon command to different levels. It also provides a mechanism for rotating the instrument at different frequencies to modulate the measured signal for the purpose of shifting the signal frequency to a lower noise region of the noise power density spectrum.

A continuous rotating centrifuge would require the use of slip rings to provide power and signal connections. Slip rings which operate reliably for long periods in a hard vacuum are non-existent. This means the device would have to be contained in a sealed pressurized container, which will cause a 5 times increase in volume, weight, and cost.

Adequate scale factor calibration can be obtained during a one cycle. This would eliminate the need for slip rings since connections can be made through a flexible cable.

Signal modulation may require rotation approaching 360° . This could also be accomplished with a reversing mechanism.

The calibration and signal modulation functions can thus both be performed by the same mechanism and command control logic.

Commands for three signal modulation rates and two calibration rates appear adequate. This would allow two input acceleration levels for use on two different scales or generate a Δg input on a single scale since:

$$\text{Scale factor } (K_s) = \frac{\text{change in input } (\Delta g)}{\text{change in output } (\Delta V)}$$

The accuracy of the calibration centrifuge is determined by the accuracy of the frequency of rotation and the stability of the radius between the rotation axis and the accelerometer proof mass center of gravity. The input acceleration is expressed by $A = \omega^2 R$, where A is acceleration, ω^2 is the angular velocity, and R is the radius.

Unlike the accelerometer scale factor, both ω and R can be maintained and known to a high degree of accuracy in orbit. The rate (ω) will be controlled by a drive frequency which may have a source accuracy of 10 ppm or better. If an accurate clock source is available on the satellite, it would be used. If not, the accelerometer would incorporate its own source.

The accuracy of R will be determined by ground measurement and would only be subject to variations in orbit due to temperature. The temperature coefficient of R can also be determined to a high degree of accuracy on the ground and is a repeatable function in orbit since only simple metal coefficients of expansion are involved.

The accuracy of R can be determined to within .001 inch, by actual measurement and to .0005 inch by using the accelerometer output as an indicator for two known rotation rates.

The temperature coefficients will be verified by using the same technique.

The overall calibration accuracy is thus determined by the degree to which R is known in flight and is expected to be in the order of .005% for R = 2 inches.

E. Satellite Interface

The location, mechanical, electrical and thermal design of the accelerometer will be influenced to a very large degree by the satellite interface constraints.

In most applications the satellite generated acceleration noise and motion effects can be minimized by locating the accelerometer at the vehicle center of gravity. This location should be determined early during the NTS-3 satellite design effort.

A. Electrical

The electrical interface will describe power, command, telemetry, and EMI requirements. The planned accelerometer design is based on currently available information in these areas.

1. Power

The satellite will supply 27 ± 1 volt dc regulated power. The accelerometer system can normally operate with $\pm 5\%$ input voltage changes without the use of an internal regulator. This usually results in a savings of 1 to 2 watts depending on regulator efficiency and final power consumption. The 12 watts which have been allocated for the accelerometer are considered sufficient.

The power conversion section of the accelerometer consists of an EMI filter followed by a transformer isolated DC to AC inverter. The secondary voltages of the inverter transformer are then rectified and filtered. All individual circuit boards employ an additional RC filter at the point where the voltage enters the board.

Experience on numerous satellites had resulted in development of an EMI filter which meets most military specifications.

To further reduce internal electric noise the EMI filter and power conversion circuits will be housed within a separate metal enclosed subassembly using feedthrough filters on all input and output leads.

The EMI filter uses high and low frequency series indicators and shunt capacitors. A series diode provides protection against polarity reversal and large negative voltage spikes. A zener diode across the line provides protection against large positive voltage spikes.

2. Commands

It is assumed that up to 10 discrete commands are available for the accelerometer system. A tentative command assignment was made to show what is considered the maximum requirement.

<u>Command Number</u>	<u>Function</u>
1	Power ON
2	Power OFF
3	Calibrate Mode 1
4	Calibrate Mode 2
5	Signal Mod. Freq. 1
6	Signal Mod. Freq. 2
7	Signal Mod. Freq. 3
8	Auto Range
9	Range A
10	Range B

The command electrical interface uses double pole double throw latching relays. This would apply to all functions except the number 1 and 2 power commands, which are usually supplied by the spacecraft, but could be contained within the system if required. There are several advantages to using latching relays. All modes of operation may be preset to the desired state prior to power application, no power is consumed except for the short duration of the command pulse, a high immunity to noise, a large number of power and signal circuits may be activated without any loading or contact resistance considerations.

A series "steering" and two shunt "suppression" diodes are included for circuit isolation. It is recommended that the command return line be isolated from both power and signal returns in the satellite.

3. Telemetry

The basic telemetry requirement for the accelerometer is transmission of the output signal to the ground.

The output signal is available on a single line pair as a serial digital word. The signal contains all the acceleration data, polarity, range and operating mode information.

Figure VII-6 shows a typical design used for this type of signal. The final circuit design will be determined by the satellite telemetry system input requirement. The output drivers and receiver design is flexible and has not presented any major difficulty in the past.

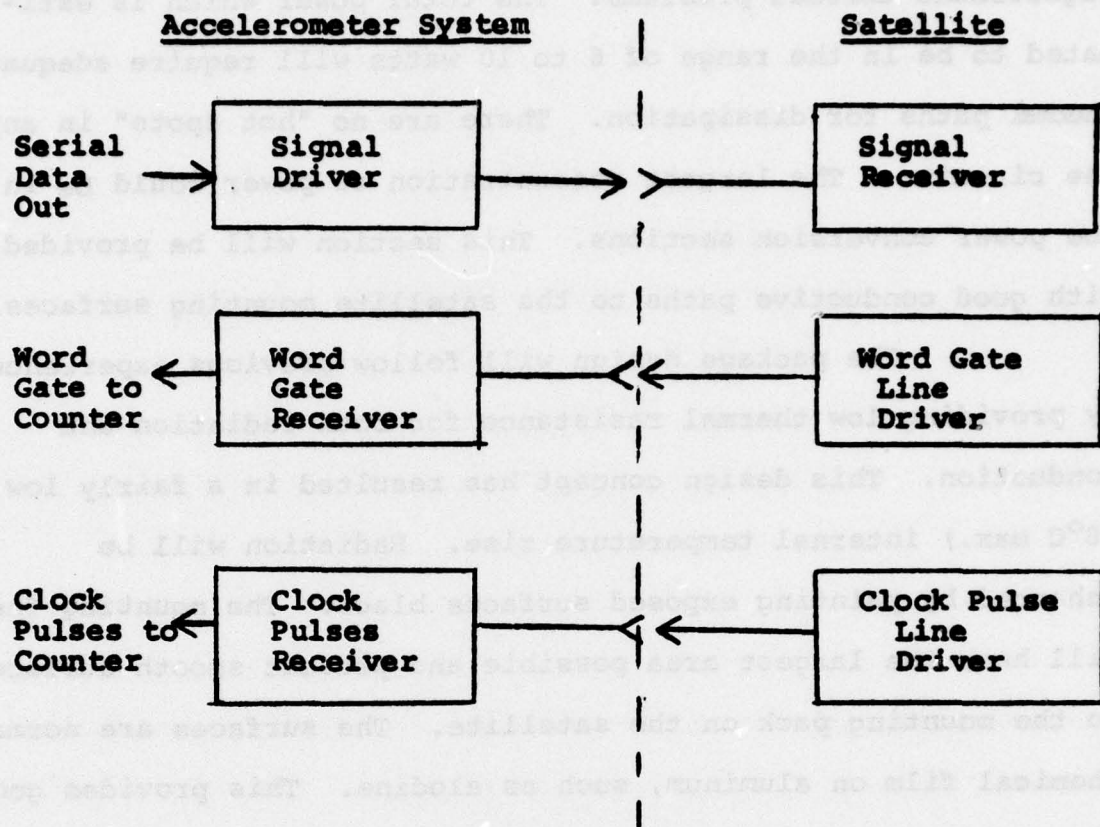


Figure VII-6. Telemetry Interface Circuit

B. Thermal

The accelerometer system should not present any significant thermal problems. The total power which is estimated to be in the range of 6 to 10 watts will require adequate thermal paths for dissipation. There are no "hot spots" in any of the circuits. The largest concentration of power would be in the power conversion sections. This section will be provided with good conductive paths to the satellite mounting surfaces.

The package design will follow previous experience by providing low thermal resistance for both radiation and conduction. This design concept has resulted in a fairly low (8°C max.) internal temperature rise. Radiation will be enhanced by painting exposed surfaces black. The mounting feet will have the largest area possible and present smooth surfaces to the mounting pack on the satellite. The surfaces are normally chemical film on aluminum, such as alodine. This provides good electrical as well as thermal contact.

After the accelerometer system location within the satellite is determined, thermal design requirements will be reviewed in detail.

The anticipated operating range of $+10^{\circ}\text{C}$ to $+30^{\circ}\text{C}$ (50°F to 86°F) is well within the limits of all electronics and mechanical components.

At this time there are no plans for heaters of any type. Scale factor and bias temperature coefficients will be accounted for during in-flight calibrations.

C. Environmental and Structural

The environments which the accelerometer system is expected to experience during transportation, handling and storage, pre-launch, ascent, and orbit operation will be considered in its design. The design will insure structural integrity of the system during or following exposure to these environments.

1. Transportation, Handling and Storage

It is anticipated that the accelerometer system will be hand-carried during transportation between the various test facilities except for final satellite installation and transportation to the launch site. A special foam padded carrying case will be provided during transportation. The case will permit ready access for airline inspection and allow handling by a single person. The maximum loads in any axis are not expected to exceed 3 g's during normal handling and transportation in the carrying case.

2. Pre-launch Environment

Pre-launch environments are not expected to be severe. Complete environmental data is not available at this time. The environments which will be specified for this period are humidity, temperature, contamination, and handling shock.

3. Ascent (Launch) Environment

The major ascent environments to be considered are vibration and rapid pressure reduction.

The mechanical design will consider the qualification testing levels as the criteria for maintaining structural and performance integrity.

Qualification levels for NTS-3 have been specified as follows:

<u>Frequency (Hz)</u>	<u>Random Vibration PSD (g^2/Hz)</u>
2	.007
2 to 100	rising at 6 db/oct to 0.170
100 to 2000	0.170

Overall level is 18.5 g's rms for a duration of 3 minutes in each axis.

In addition to vibration, the unit will be designed to withstand pyro shock levels of 2000 g's peak.

The use of packaging techniques which have been proven by test on previous designs will be utilized. The NTS-3 qualification levels are well within previous limits.

The design will also make provisions for venting the unpressurized portions of the system at a rate compatible with ascent pressure reduction. In most cases, a small vent hole is added if the normal leakage around connector brackets, or cover/base interface does not provide sufficient volume.

D. Mechanical

The accelerometer system packaging is flexible enough to permit either a single or dual unit system design.

The requirement for rotating the instrument and desirability of locating it near the satellite center of gravity favors the use of a two package system. The accelerometer and its

pick-off electronics would be mounted on the rotating base or centrifuge portion. The balance of the constraint loops, interface electronics and centrifuge drive signals would be located in a separate electronics package. An estimate of size and weight was made based on previous experience and without the benefit of detailed knowledge of the satellite mechanical and electrical interface constraints.

The accelerometer and centrifuge package would have a 6 x 6 inch square mounting base with a total height of 6-1/4 inches. Weight is estimated at 8 lbs. maximum.

The electronics package is estimated to have dimensions of 7" long, 5" wide, and 3-1/2" high. Its estimated weight is 3-1/2 lbs.

An interconnecting cable will be supplied if required. It is, however, recommended that the satellite manufacturer fabricate the cable and install it using volume models with actual connectors installed as a guide.

F. Ground Support Equipment

Ground Support Equipment (GSE) is intended to: (1) simulate the satellite/accelerometer electrical interface by providing identical load/source impedance and signal levels to those in the satellite, and (2) serve as special test equipment by providing 1 g constraint capability to verify performance to specification during all phases of testing before and after delivery. This would include environmental and prelaunch tests at the satellite integration facility and launch site.

The GSE will be portable and packaged to allow airline inspection as carry-on luggage. It will contain only those circuits and functions which cannot be provided by readily available test equipment.

Figure VII-7 is a block diagram of the GSE. Two regulated power supplies are used. One simulates the satellite's 27 volt supply. The power control and monitoring circuit consists of a front panel toggle switch, voltage and current meters plus test points for convection of an internal variable supply.

A separate 10 volt regulated supply powers all circuits within the GSE.

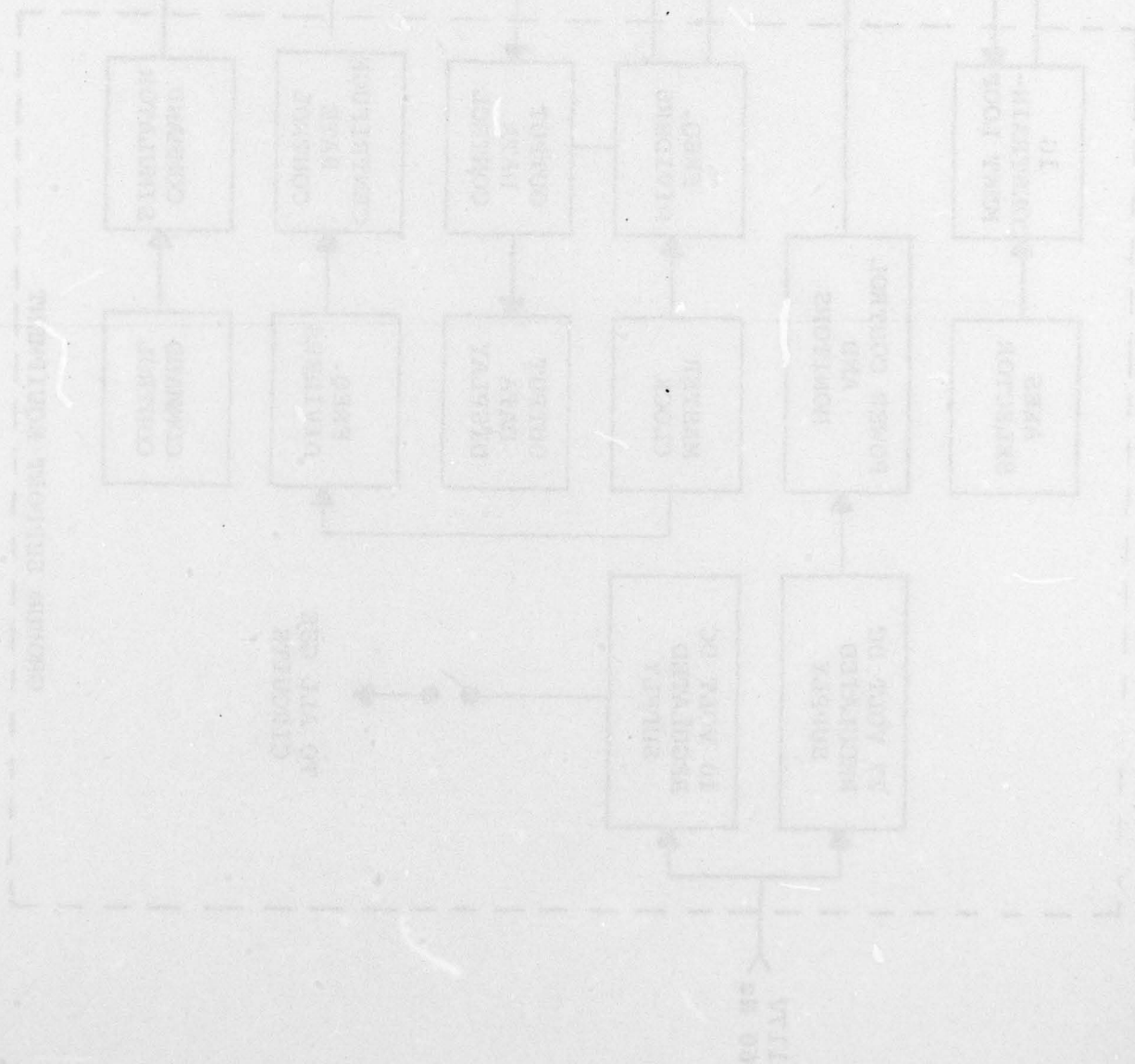
A master clock circuit provides the basic signal source for the digital output data and also controls the centrifuge rate. Internally it will also provide means for observing the output data word.

The command section simulates the satellite command output circuits and is controlled by front panel switches.

The 1 G constraint loop can be switched to whichever axis is vertical during ground tests.

Included as part of the GSE will be test cables and a tilt fixture for individual axes tests. Figure VII-8 shows connections for a typical functional test at a field site.

Test procedures will require the system level use of the GSE so standard comparable test conditions are provided at all times.



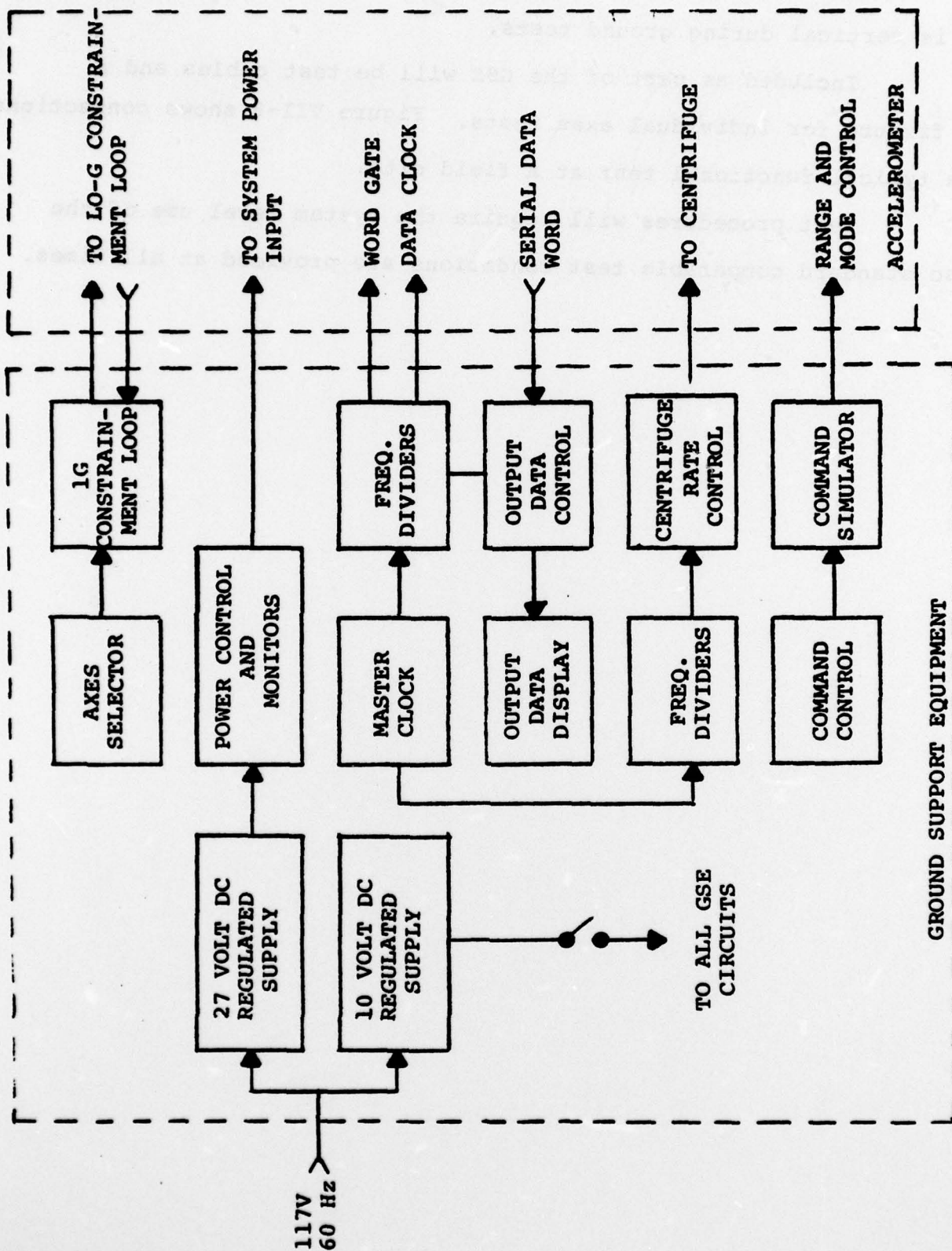


Figure VII-7. Block Diagram Ground Support Equipment (GSE)

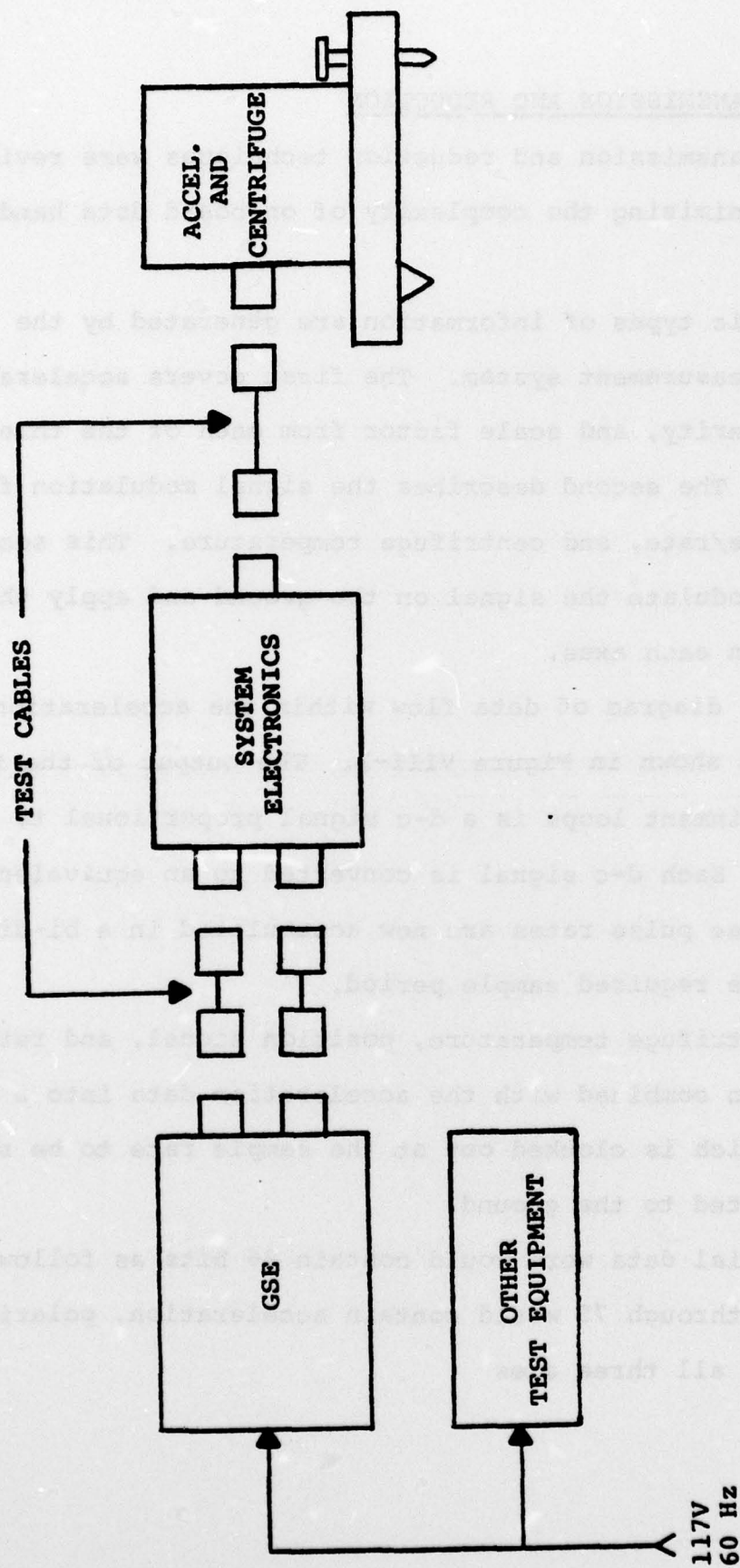


Figure VII-8. Typical Functional Test Connection

VIII. DATA TRANSMISSION AND REDUCTION

Data transmission and reduction techniques were reviewed with the goal of minimizing the complexity of on-board data handling hardware.

Two basic types of information are generated by the acceleration measurement system. The first covers acceleration magnitude, polarity, and scale factor from each of the three sensing axes. The second describes the signal modulation frequency, centrifuge mode/rate, and centrifuge temperature. This second type is used to demodulate the signal on the ground and apply the correct scale factor in each axes.

A block diagram of data flow within the acceleration measurement system is shown in Figure VIII-1. The output of the three analog constraint loops is a d-c signal proportional to input acceleration. Each d-c signal is converted to an equivalent pulse rate. The three pulse rates are now accumulated in a bi-directional counter for the required sample period.

The centrifuge temperature, position signal, and rate signal are then combined with the acceleration data into a single serial word which is clocked out at the sample rate to be stored until transmitted to the ground.

The serial data word would contain 96 bits as follows:

Bits 1 through 75 would contain acceleration, polarity, and scaling on all three axes.

Acceleration X Axis	22
Acceleration Y Axis	22
Acceleration Z Axis	22
Polarity X,Y,Z	3
scaling X,Y,Z	<u>6</u>
TOTAL	75

Bits 76 through 96 would contain centrifuge temperature, rate, and position.

Temperature	8
Rate	4
Position	<u>4</u>
TOTAL	16

Assuming a 300 second sample time, the 4K bit satellite storage would be filled in 41 data words or approximately every 3.5 hours.

If the orbit period is 12 hours and only 1 dump per orbit is practical, then the data bits would have to be reduced to 24 bits per word as compared to the proposed 96.

Data compression technique to accomplish this will be considered but are beyond the scope of this study.

One method is to transmit only bits which change from the previous sample. Most of the centrifuge data could be expected to be constant for 10 or more sample periods. Polarity and scaling would also be nearly constant. The acceleration data would experience the most change. In this case only changing bits would be transmitted.

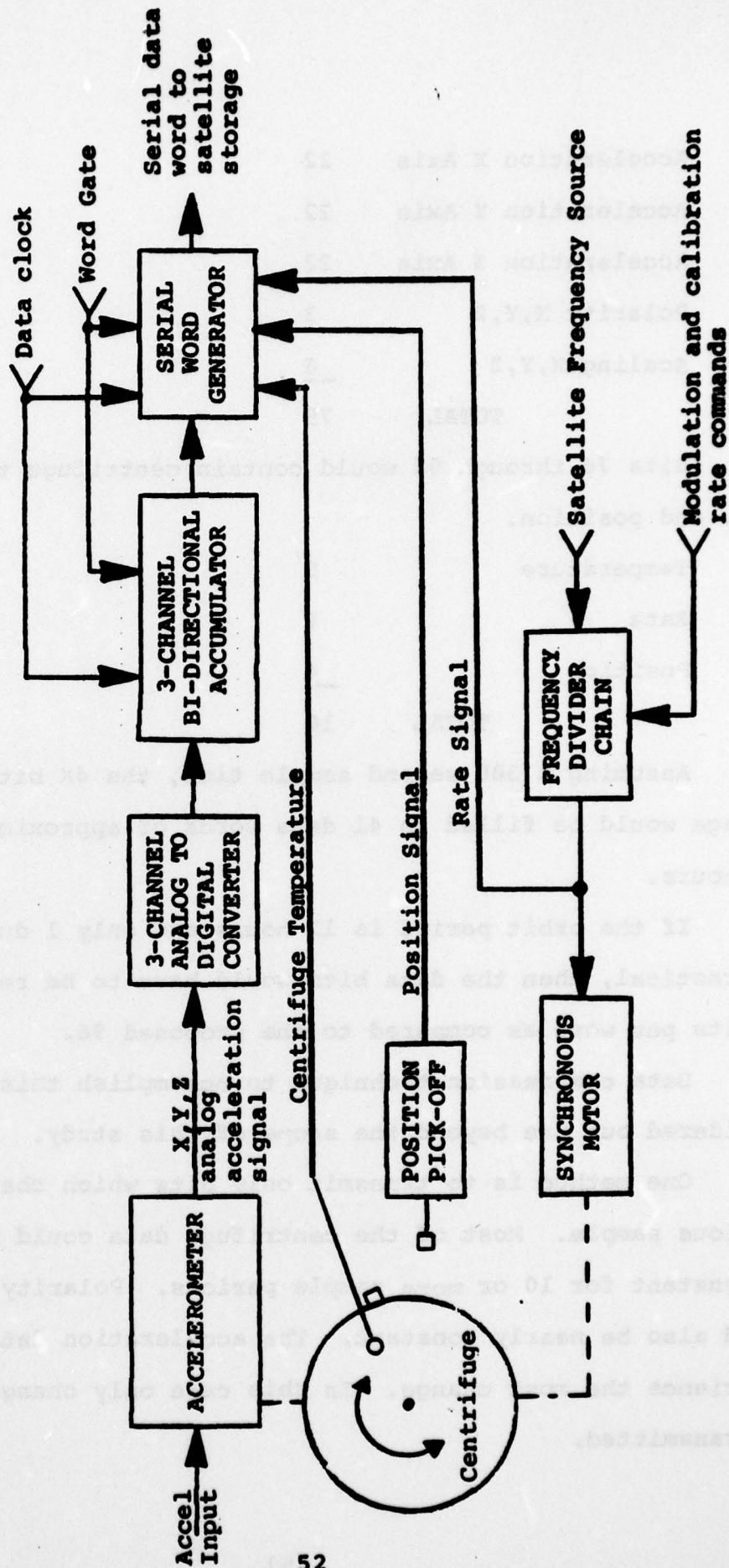


Figure VIII-1. Accelerometer System Data Flow

APPENDIX A

MESA ACCELERATION ALGORITHM

The MESA's accelerometer's proof mass is connected to the NTS-3 vehicle through a constraint system in which three axes of acceleration are measured. This appendix develops the algorithm for these measured acceleration components.

Assuming the NTS-3 vehicle is a rigid body, a force vector diagram of the vehicle/accelerometer system in a fixed reference frame can be constructed as shown in Figure A-1.

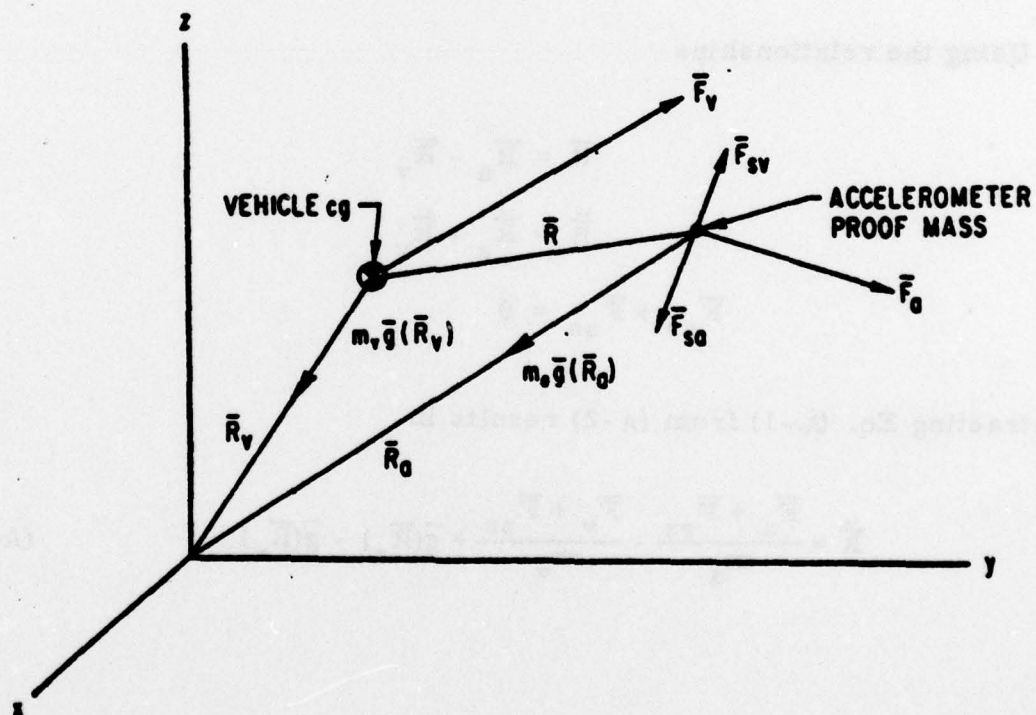


FIGURE A-1. Force Vector Diagram

The symbols in Fig. A-1 are defined as follows:

- \bar{R}_i = radius vector from the earth center to i (i = v, a)
- \bar{F}_i = vector sum of external forces applied to i (i = v, a;
 \bar{F}_a represents accelerometer bias term)
- \bar{F}_{si} = suspension force vector (i = v, a)
- $m_i \bar{g}(\bar{R}_i)$ = gravity force vector (i = v, a)

From these definitions, the acceleration equation for each mass is

$$\ddot{\bar{R}}_v = \frac{\bar{F}_v + \bar{F}_{sv}}{m_v} + \bar{g}(\bar{R}_v) \quad (A-1)$$

$$\ddot{\bar{R}}_a = \frac{\bar{F}_a + \bar{F}_{sa}}{m_a} + \bar{g}(\bar{R}_a) \quad (A-2)$$

Using the relationships

$$\bar{R} = \bar{R}_a - \bar{R}_v$$

$$\ddot{\bar{R}} = \ddot{\bar{R}}_a - \ddot{\bar{R}}_v$$

$$\bar{F}_{sv} + \bar{F}_{sa} = 0$$

and subtracting Eq. (A-1) from (A-2) results in

$$\ddot{\bar{R}} = \frac{\bar{F}_a + \bar{F}_{sa}}{m_a} - \frac{\bar{F}_v + \bar{F}_{sa}}{m_v} + \bar{g}(\bar{R}_a) - \bar{g}(\bar{R}_v) \quad (A-3)$$

Assuming the accelerometer mass is negligible with respect to the vehicle mass, the acceleration sensed by the accelerometer's force suspension system is

$$\frac{\bar{F}_{sa}}{m_a} = \frac{\bar{F}_v}{m_v} + \ddot{\bar{R}} - [\bar{g}(\bar{R}_a) - \bar{g}(\bar{R}_v)] - \frac{\bar{F}_a}{m_a} \quad (A-4)$$

The acceleration vector $\ddot{\bar{R}}$ expressed in the rotating vehicle axis frame is

$$\ddot{\bar{R}} = \ddot{\bar{r}} + \bar{\omega} \times (\bar{\omega} \times \bar{r}) + \dot{\bar{\omega}} \times \bar{r} + 2\bar{\omega} \times \dot{\bar{r}} \quad (A-5)$$

where $\bar{\omega}$ and $\dot{\bar{\omega}}$ are the inertial angular rate and acceleration vectors, respectively, of the vehicle axes and \bar{r} is the displacement vector expressed in body axes coordinates. Neglecting the bias term (\bar{F}_a/m_a) , changing the symbols of the force to mass terms, and using the symbol $\bar{g}(\bar{r})$ for the gravity gradient term results in the following equation for the sensed acceleration vector expressed in body axis coordinates

$$\bar{A}_s = \bar{A}_{cg} + \ddot{\bar{r}} + \bar{\omega} \times (\bar{\omega} \times \bar{r}) + \dot{\bar{\omega}} \times \bar{r} + 2\bar{\omega} \times \dot{\bar{r}} - \bar{g}(\bar{r}) \quad (A-6)$$

where

$$\bar{r} = \begin{pmatrix} X_{ag} + r_a \cos \phi_t \\ Y_{ag} + r_a \sin \phi_t \\ Z_{ag} \end{pmatrix}$$

instantaneous coordinates of proof mass with respect to the vehicle cg (see Fig. 1)

$$\bar{\omega} = \begin{pmatrix} \omega_x \\ \omega_y \\ \omega_z \end{pmatrix}$$

Inertial body rates

$\bar{g}(\bar{r})$ = gravity gradient term (see below)

Since the coordinates of the NTS-3 package with respect to the cg (X_{ag} , Y_{ag} , Z_{ag}) and the turntable radius arm r_a are assumed constant, the relative velocity and acceleration of the proof mass are

$$\dot{\vec{r}} = r_a \dot{\phi}_t \begin{pmatrix} -\sin \phi_t \\ \cos \phi_t \\ 0 \end{pmatrix} \quad (A-7)$$

$$\ddot{\vec{r}} = -r_a \dot{\phi}_t^2 \begin{pmatrix} \cos \phi_t \\ \sin \phi_t \\ 0 \end{pmatrix} + r_a \ddot{\phi}_t \begin{pmatrix} -\sin \phi_t \\ \cos \phi_t \\ 0 \end{pmatrix} \quad (A-8)$$

and

$$\dot{\vec{\omega}} = \begin{pmatrix} \dot{\omega}_x \\ \dot{\omega}_y \\ \dot{\omega}_z \end{pmatrix} \quad (A-9)$$

The gravity gradient term is developed assuming a spherical earth as follows:

$$\begin{aligned} \vec{g}(\vec{R}_v) &= -\frac{\mu}{R_v^3} \vec{R}_v \\ \vec{g}(\delta \vec{R}) &= \frac{\mu}{R_v^3} \left[\frac{3\vec{R}_v \vec{R}_v^T}{R_v^2} - \mathbf{I} \right] \delta \vec{R} = \omega_o^2 \begin{bmatrix} -1 & 0 & 0 \\ 0 & -1 & 0 \\ 0 & 0 & 2 \end{bmatrix} \delta \vec{R} \end{aligned}$$

where

$$\bar{R}_v = \begin{pmatrix} 0 \\ 0 \\ -Z \end{pmatrix}$$

radius vector from the earth center to the NTS-3 cg expressed in orbit plane coordinates*

$$\delta \bar{R} = \begin{pmatrix} \delta X \\ \delta Y \\ \delta Z \end{pmatrix}$$

displacement coordinates from the cg expressed in orbit plane coordinates

$$\omega_o = -(\mu/R_v^3)^{1/2} \quad \text{instantaneous orbital rate}$$

The body axis system is related to the orbit axis system by

$$\begin{pmatrix} x \\ y \\ z \end{pmatrix}_b = \begin{bmatrix} 1 & 0 & 0 \\ 0 & \cos \varphi & \sin \varphi \\ 0 & -\sin \varphi & \cos \varphi \end{bmatrix} \begin{bmatrix} \cos \psi & \sin \psi & 0 \\ -\sin \psi & \cos \psi & 0 \\ 0 & 0 & 1 \end{bmatrix} \begin{bmatrix} \cos \theta & 0 & -\sin \theta \\ 0 & 1 & 0 \\ \sin \theta & 0 & \cos \theta \end{bmatrix} \begin{pmatrix} x \\ y \\ z \end{pmatrix}_o$$

where

θ, ψ, φ = ordered rotations (pitch, yaw, roll) of the NTS-3 vehicle axis with respect to the orbit plane axis.

When it is assumed that the angles (θ, ψ, φ) are small ($\cos = 1$, $\sin = \text{angle}$, $\sin \text{ products} = 0$), the order of rotations is immaterial and the transformation reduces to a skew symmetric matrix

$$\begin{pmatrix} x \\ y \\ z \end{pmatrix}_b = \begin{bmatrix} 1 & \psi & -\theta \\ -\psi & 1 & \varphi \\ \theta & -\varphi & 1 \end{bmatrix} \begin{pmatrix} x \\ y \\ z \end{pmatrix}_o = M_{bo} \begin{pmatrix} x \\ y \\ z \end{pmatrix}_o$$

* In the orbit plane coordinate system, the z axis is directed along the negative radius vector, the y axis is directed normal to the orbit plane, and the x axis is directed forward, forming a right-hand system.

With the above definitions, the gravity gradient term is

$$\begin{aligned}\bar{g}(\bar{r}) &= M_{bo} \bar{g}(\delta \bar{R}) \\ &= \omega_o^2 M_{bo} \begin{bmatrix} -1 & 0 & 0 \\ 0 & -1 & 0 \\ 0 & 0 & 2 \end{bmatrix} M_{bo}^T \bar{r} \\ &= \omega_o^2 \begin{bmatrix} -1 & 0 & -3\theta \\ 0 & -1 & 3\varphi \\ -3\theta & 3\varphi & 2 \end{bmatrix} \bar{r}\end{aligned}$$

Substituting Eqs. (A-7), (A-8), (A-9), and (A-10) into Eq. (A-6) and collecting terms results in the following x and y components of vehicle acceleration

$$\begin{aligned}A_{sx} &= A_{xcg} - r_a \{ \cos \phi_t [(\dot{\phi}_t + \omega_z)^2 + \omega_y^2 - \omega_o^2] + \sin \phi_t (\ddot{\phi}_t + \dot{\omega}_z - \omega_x \omega_y) \} \\ &\quad - X_{ag}(\omega_y^2 + \omega_z^2 - \omega_o^2) - Y_{ag}(\dot{\omega}_z - \omega_x \omega_y) + Z_{ag}(\omega_x \omega_z + \dot{\omega}_y + 3\omega_o^2 \theta)\end{aligned}$$

$$\begin{aligned}A_{sy} &= A_{ycg} - r_a \{ \sin \phi_t [(\dot{\phi}_t + \omega_z)^2 + \omega_x^2 - \omega_o^2] + \cos \phi_t (-\ddot{\phi}_t - \dot{\omega}_z - \omega_x \omega_y) \} \\ &\quad - X_{ag}(\omega_x \omega_y - \dot{\omega}_z) - Y_{ag}(\omega_x^2 + \omega_z^2 - \omega_o^2) - Z_{ag}(\dot{\omega}_x - \omega_y \omega_z + 3\omega_o^2 \varphi)\end{aligned}$$

The "X" axis acceleration input to the MESA accelerometer when rotated at a rate $\dot{\phi}_t$ in the X-Y plane (rotation axis is Z axis)...

$$A_x = A_{sx} \cos \phi_t + A_{sy} \sin \phi_t$$

Performing the above transformation and collecting terms results in

$$\begin{aligned}
 A_x = & A_{xcg} \cos \phi_t + A_{ycg} \sin \phi_t - r_a [(\dot{\phi}_t + \omega_z)^2 + (\cos \phi_t \omega_y - \sin \phi_t \omega_x)^2 - \omega_o^2] \\
 & + X_{ag} [\sin \phi_t (\dot{\omega}_z + \omega_x \omega_y) - \cos \phi_t (\omega_y^2 + \omega_z^2 - \omega_o^2)] \\
 & + Y_{ag} [\cos \phi_t (\omega_x \omega_y - \dot{\omega}_z) - \sin \phi_t (\omega_x^2 + \omega_z^2 - \omega_o^2)] \\
 & + Z_{ag} [\cos \phi_t (\omega_x \omega_z + \dot{\omega}_y + 3\omega_o^2 \theta) - \sin \phi_t (\dot{\omega}_x - \omega_y \omega_z + 3\omega_o^2 \varphi)] \quad (A-11)
 \end{aligned}$$

The "Y" axis acceleration input to the MESA is

$$A_y = A_{sx} \sin \phi_t + A_{sy} \cos \phi_t$$

which is the same as A_x with $\sin \phi_t$ and $\cos \phi_t$ interchanged.

The "Z" axis acceleration input is

$$\begin{aligned}
 A_z = & A_{zcg} - r_a [\cos \phi_t (\dot{\omega}_y + \omega_o^2 3\theta - 2\omega_x \dot{\phi}_t - \omega_x \omega_z) \sin \phi_t (2\omega_y \dot{\phi}_t + \omega_y \omega_z + \dot{\omega}_x + \omega_o^2 3\phi) \\
 & - X_{ag} [\dot{\omega}_y + \omega_o^2 3\theta - \omega_x \omega_z] \\
 & + Y_{ag} [\omega_y \omega_z + \dot{\omega}_x + \omega_o^2 3\phi] \\
 & - Z_{ag} [\omega_x^2 + \omega_y^2 - 2\omega_o^2]
 \end{aligned}$$